Lithos xxx (2012) xxx–xxx

Contents lists available at SciVerse ScienceDirect

Lithos

journal homepage: www.elsevier.com/locate/lithos

Geochronology and geochemistry of the Essimingor volcano: Melting of metasomatized lithospheric mantle beneath the North Tanzanian Divergence zone (East African Rift)

S. Mana [a,*], T. Furman [b], M.J. Carr [a], G.F. Mollel [c], R.A. Mortlock [a], M.D. Feigenson [a], B.D. Turrin [a], C.C. Swisher III [a]

[a] Department of Earth and Planetary Sciences, Rutgers University, NJ 08854, USA
[b] Department of Geosciences, Pennsylvania State University, University Park, PA 16802, USA
[c] Department of Earth and Atmospheric Sciences, University of Alberta, Edmonton, Canada T6G 2N8

ARTICLE INFO

Article history:
Received 9 May 2012
Accepted 23 September 2012
Available online xxxx

Keywords:
North Tanzanian Divergence
$^{40}Ar/^{39}Ar$ dating
Lead isotope
Neodymium isotope
Strontium isotope

ABSTRACT

The North Tanzanian Divergence zone (NTD), at the southern end of the eastern branch of the East African Rift, is part of one of Earth's few currently active intra-continental rift systems. The NTD preserves a complex tectono-magmatic evolution of a rift in its early stage of activity. The oldest magmatism reported in the NTD is associated with the centrally located Essimingor volcano. Although major element oxides show narrow compositional variations suggesting fractional crystallization, trace element abundances and Sr–Nd–Pb isotopic data have complex distributions that require open-system processes. The more primitive samples (MgO > 9 wt.%) likely reflect partial melting of a metasomatized lithospheric mantle characterized by residual garnet, phlogopite and minor amphibole. The range of radiogenic Pb isotopic compositions indicates the presence of mixing between this source and the lithosphere of the western branch of the East African Rift (Toro Ankole and Virunga). Laser-incremental heating of selected samples gives $^{40}Ar/^{39}Ar$ ages that range from 5.76 ± 0.02 Ma to 5.91 ± 0.01 Ma, suggesting an age roughly 2 myr younger than previously reported.

1. Introduction

The East African Rift (EAR) is an intracontinental rift system characterized by a succession of extensional basins linked and segmented by accommodation zones (Chrorowicz, 2005). Volcanism in the EAR is considered to be a result of one or more mantle plumes from undetermined depths of origin rising to the base of the lithosphere (e.g. Ebinger and Sleep, 1998; George et al., 1998; Lin et al., 2005; Nyblade et al., 2000; Owens et al., 2000; Smith, 1994). Along the length of the EAR, numerous volcanoes with highly variable volumes and compositions have erupted both prior to and in conjunction with the onset of documented extension at ~30 Ma (Baker et al., 1996; Hofmann et al., 1997). The age, duration and geochemical evolution of these volcanoes serve as primary bases for unraveling the tectonomagmatic development and history of the EAR.

In northern Tanzania, magmatic activity and rifting are superimposed upon a pre-existing zone of crustal weakness: the tectonic contact between the Archean Tanzanian Craton to the west and the Proterozoic Mozambique Mobile Belt to the east (Smith, 1994; Fig. 1). Baker et al. (1972) referred to this region as the North Tanzanian Divergence zone (NTD). The earliest occurrence of volcanism in the NTD appears to be Late Miocene or Early Pliocene, thus much younger than in the northern part of the EAR. The NTD is characterized by an abrupt widening of the rift at around 3°S where it extends from the Plio-Quaternary Kilimanjaro volcano in the east to the large Late Pleistocene caldera of Ngorongoro in the west (Fig. 1). This 200 km wide zone contrasts markedly with the 50–60 km width of the majority of the East African Rift, and is comparable to the width observed in Turkana, northern Kenya. From north to south, the NTD volcanoes (Fig. 1) include the poorly studied Gelai near the Kenya–Tanzania border, and the nearby well-known Oldoinyo Lengai, Earth's only active carbonatite volcano; southward, the Late Miocene Essimingor volcano is considered the oldest pre-rift volcano of the NTD based on a K–Ar age of around 8 Ma from Bagdasaryan et al. (1973). The present day north–south rift valley in the NTD is thought to have been established about 1.2 Ma (MacIntyre et al., 1974) and the older volcanoes to have erupted in a pre-rift tectonic depression (Dawson, 1992).

The detailed geochemical, spatial and temporal evolution of the NTD remains unclear, due to a lack of sampling, geochemical and geochronological data (see summaries in Dawson, 2008 and Le Gall et al., 2008). The age data are highly variable in quality and many are isolated K–Ar dates. To address these uncertainties and to better unravel the tectonomagmatic history of the NTD, we have initiated a systematic program focused on providing detailed geochemical and geochronological

* Corresponding author at: Earth and Planetary Sciences, Rutgers University, 610 Taylor Road, Piscataway, NJ 08854, USA. Tel.: +1 732 445 2044; fax: +1 732 445 3374.
E-mail address: manasara@eden.rutgers.edu (S. Mana).

0024-4937/$ – see front matter © 2012 Elsevier B.V. All rights reserved.
http://dx.doi.org/10.1016/j.lithos.2012.09.009

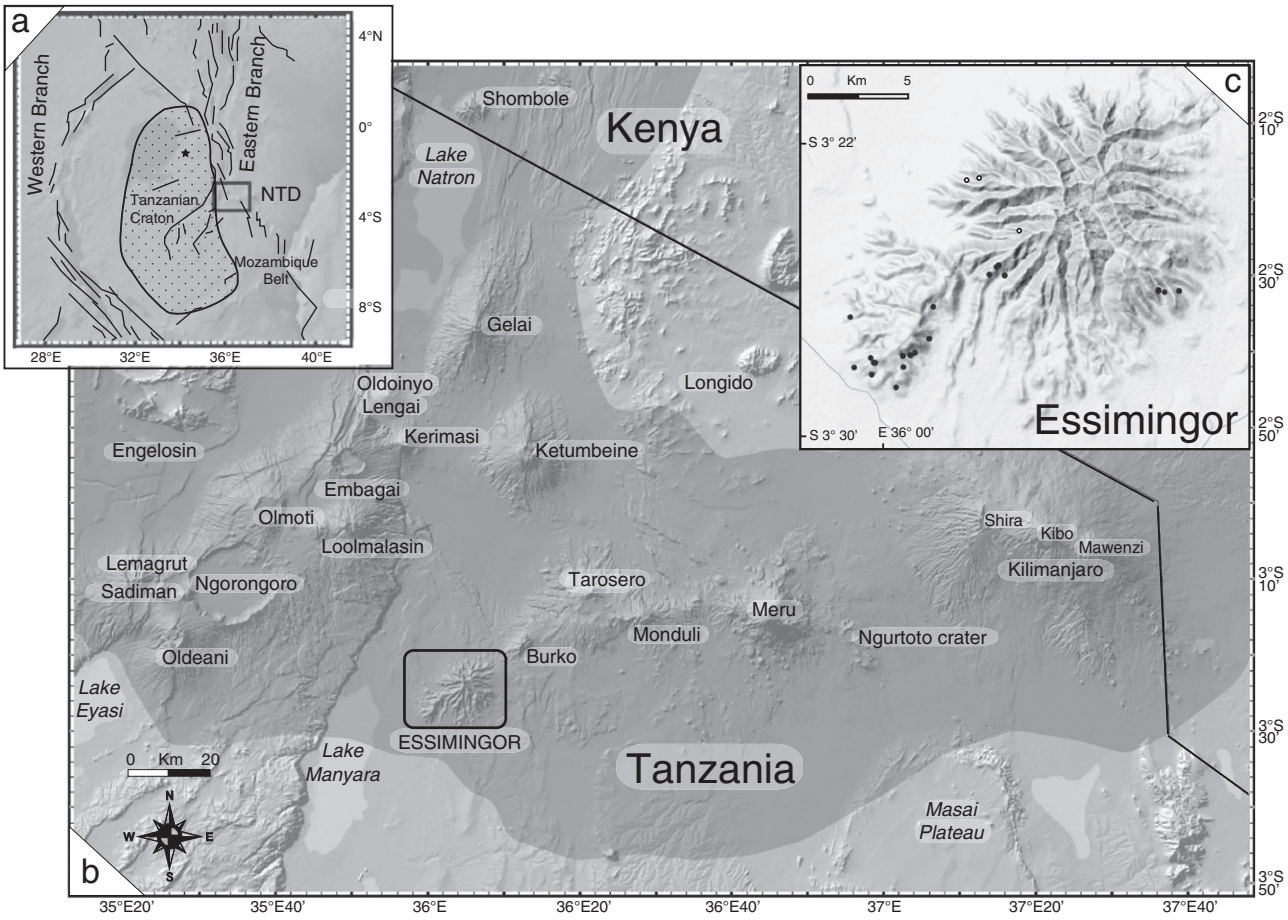

Fig. 1. (a) Map of the southern sector of the East African Rift showing major regional faults, including the boundary between the Archean Tanzanian Craton and the Proterozoic Mozambique Belt and location of the North Tanzanian Divergence (Chrorowicz, 2005; Nyblade et al., 2000). The black star represents the location of the crustal contaminant used in the discussion (TA-47, Manya et al., 2007). (b) Map of the North Tanzanian Divergence sector of the East African Rift. The shaded area represents the Neogene to Recent volcanism as in Dawson (1992). (c) Essimingor volcano and the location of the samples selected in this study (inclusive of Paslick et al., 1995 location: BD214 (3°23′6″S, 36°2′15″E), BD216 (3°23′6″S, 36°2′36″E) and BD247 (3°24′30″S, 36°3′40.7″E) from Dawson personal communication).
Map modified from GeoMapApp and CNES/SPOT image 2010.

data for key northern Tanzanian volcanoes (Mollel et al., 2008, 2009, 2011). Here, we report our findings on the centrally located Essimingor volcano, which likely record the earliest volcanic activity in the NTD.

2. This study

We collected 40 well-located lava samples from the S–SW slopes of Essimingor volcano (Fig. 1, Table 1). Samples are not evenly distributed across the volcano because of access difficulties; nevertheless an attempt was made to collect a variety of lithologies among the visible range of lava types in the area. Unfortunately a geologic map of the volcano is not available and due to the extensive vegetation we were unable to produce a stratigraphic section of the samples collected. We report here the results of $^{40}Ar/^{39}Ar$ dating, major and trace element analyses, and Pb, Sr, and Nd isotope analyses for the Essimingor samples. In the laboratory, thin sections were made to determine phenocryst assemblages and degree of weathering (summary available in Appendix A). Twenty two samples were further prepared for geochemical analyses, and 12 of these were dated by $^{40}Ar/^{39}Ar$ geochronology.

3. Background and methods

3.1. Geochronology

Evans et al. (1971) reported four K–Ar analyses (replicates on two samples) of nephelinite collected from one location on the southeast slopes of Essimingor. The ages are 4.89 ± 0.09 and 4.68 ± 0.09 Ma for one sample, and 3.23 ± 0.07 and 3.20 ± 0.06 Ma for the other. Based on these data Evans et al. (1971) concluded that Essimingor was active during the Pliocene, probably before 4.8 Ma. Bagdasaryan et al. (1973) reported two additional K–Ar analyses from Essimingor based on a single whole rock sample of melaphonolite lava. The precise location on Essimingor from where this sample was collected is not known. Duplicate K–Ar analyses of this sample yielded ages of 8.1 ± 1 Ma and 7.35 ± 0.65 Ma. These K–Ar dates are commonly used to establish Essimingor as the oldest volcano of the NTD (e.g. Dawson, 2008; Le Gall et al., 2008).

Whole rock, matrix, and when possible, nepheline separates were analyzed using $^{40}Ar/^{39}Ar$ laser incremental-heating techniques for twelve selected samples (Table 2). Samples were crushed, sieved between 300 and 600 μm (50 and 30 mesh sizes), and washed with distilled water in an ultrasonic bath, loaded into wells of Al irradiation disks, wrapped in Al foil and sealed in a quartz–glass tube. The samples, along with multiple splits of the monitor mineral, Fish Canyon Sanidine (FC2 = 28.02 ± 0.16 Ma; Renne et al., 1998), were irradiated in the central thimble of the USGS TRIGA reactor in Denver for 20 min. The following interference correlations were used: $(^{36}Ar/^{37}Ar)_{Ca} = 2.64 \pm 0.02$ (10^{-4}), $(^{39}Ar/^{37}Ar)_{Ca} = 6.73 \pm 0.04$ (10^{-4}), $(^{38}Ar/^{39}Ar)_{K} = 1.34 \pm 0.02$ (10^{-2}) (Dalrymple et al., 1981, 1993). $^{40}Ar/^{39}Ar$ ages were determined in the Rutgers' Earth and Planetary Sciences Noble Gas Laboratory, following procedures similar to those described in Carr et al. (2007).

Please cite this article as: Mana, S., et al., Geochronology and geochemistry of the Essimingor volcano: Melting of metasomatized lithospheric mantle beneath the North Tanzanian Divergence zone (East African Rift), Lithos (2012), http://dx.doi.org/10.1016/j.lithos.2012.09.009

The $^{40}Ar/^{39}Ar$ results, summarized in Table 2, include integrated total fusion age, plateau age and inverse isochron age of the plateau steps. The plateau ages were calculated based on the following standard parameters: 2-sigma of error overlap, a minimum number of three continuous steps indistinguishable at a 95% confidence value, and being representative of a minimum value of 40% of the total $^{39}Ar^*$ released. The inverse isochron ages are deduced by the fit obtained from plotting the atmospheric related $^{36}Ar/^{40}Ar$ component against the radiogenic $^{39}Ar/^{40}Ar$ (McDougall and Harrison, 1999). The ages that are considered more reliable are shown in bold in Table 2.

3.2. Geochemistry

Few geochemical data for Essimingor have been published. Paslick et al. (1995) reported major and trace elements and Sr–Nd–Pb isotopic compositions for three samples described as foidite and basanite. Dawson (2008) mentions the presence of melilites and nephelinites from Essimingor as reported by Wood (1968) in an unpublished Ph.D. thesis.

We report here major and trace element abundances for 22 samples and Pb, Sr, and Nd isotopic data for 15 of them (Tables 1 and 3). Samples were crushed in a steel jaw crusher and washed with deionized water in an ultrasonic bath. Alteration-free rock chips were selected using a stereoscopic microscope and powdered using an alumina mill. At Michigan State University, the powders of 8 samples were fused into homogeneous glass disks using ~5 g of sample plus lithium tetraborate ($Li_2B_4O_7$). Analytical methods are similar to those reported by Hannan et al. (2002). Glass disks were analyzed by X-ray fluorescence (XRF) in a Bruker S4 Pioneer for major elements and selected trace elements (e.g., Ni, Rb, Sr, Zr, Zn and Cu). Trace elements were obtained subsequently on the same glass disks by laser ablation inductively coupled plasma mass spectrometry (LA-ICP-MS) in a Micromass Platform ICP-MS with a Cetac LSX 200 + Nd: YAG laser (266 nm). The other 16 samples were analyzed at Duke University. In this case, the powders were fused with a Li meta-borate flux to obtain major elements by Direct Current Plasma Optical Emission Spectrometer (DCP-OES) and acid digested to analyze trace elements by Inductively Coupled Plasma Mass Spectrometer (ICP-MS) (procedure details reported in Furman et al., 2006b).

The Pb, Sr, and Nd isotope analyses were carried out through sample digestion and element chromatography performed at Rutgers in a Class 1000 clean room, equipped with Class 100 laminar flow hoods with downdraft exhaust, using a geochemical sample preparation following procedures previously outlined in Gazel et al. (2009). About 500 mg of whole rock powder of each sample was dissolved in an open Teflon-beaker at ~150 °C, by successive steps of dissolution and acid digestion (HF, HNO_3 concentrate, 7.3 N HCl and 0.5 N HBr were used). Isotope separation and ratio determinations were resolved using a GV Isoprobe-T multicollector thermal ionization mass spectrometer (TIMS). Sr and Nd were measured in a dynamic multicollection mode, whereas Pb was measured in a static multicollection following the procedures outlined in Gazel et al. (2009). Moreover, an alternative procedure to measure Pb isotopes using a Fisons PLASMA 54 multi-collector magnetic sector double focusing Inductively Coupled Mass Spectrometer (MC-MS-ICPMS) has been adopted at Rutgers. A set of Pb analyses was performed resulting in a high quality dataset (see detailed procedure in Appendix B). The Pb isotopic data produced by TIMS were corrected for mass fractionation following the Galer and Abouchami (1998) parameters. An exponential correction based on the recent published atomic masses by Berlund and Wieser (2011) have been applied on the analyses obtained by MC-MS-ICPMS (see details in Appendix B).

4. Results

4.1. Geochronology

Laser-incremental heating $^{40}Ar/^{39}Ar$ analyses of whole rock, matrix and nepheline separates of the Essimingor lavas yield plateau ages that range from 5.76 ± 0.01 to 5.91 ± 0.01 Ma. Examples of the $^{40}Ar/^{39}Ar$ data are shown in Fig. 2. Some measurements, not considered in the final age range, show a progressive monotonic decrease of apparent ages with increasing temperature, possibly explained by a trapped argon component, ^{39}Ar recoil and/or alteration (e.g. ES10-2008 matrix, Fig. 2 bottom right). A few analyses were of low radiogenic yield, with large accompanied uncertainties (e.g. ESMT-6 whole rock, Fig. 2 bottom left) and likewise are not included (see detailed selection criteria in Table 2). Many of the analyses were highly radiogenic. In these cases, the inverse isochron plots, although showing a well-behaved mixing line yield fairly large uncertainties with the $^{40}Ar/^{36}Ar$ intercept, but small uncertainties in $^{39}Ar/^{40}Ar$ intercept, and thus the age (Fig. 3a). In some samples, such as the nepheline from ES17-2008, the inverse isochron plot (Fig. 3b) shows two components, underlining the presence of a trapped or secondary Ar component. The primary component shows an atmospheric composition within error, $^{40}Ar/^{36}Ar$ intercept of 282 ± 16. The secondary component has a $^{40}Ar/^{36}Ar$ intercept at 4000 ± 3000. The resultant age of the primary component is still considerably older than the range of the other samples. This can be due to an incomplete resolution of the two components or a further contamination not clearly identified here. For this reason samples presenting this behavior were not included in the final age range. Nepheline separates from some of our dated samples yield anomalously old integrated ages (K–Ar equivalent) and were discarded as well (Table 2). Of the twelve samples dated, six provide reliable ages and two of these (ESMT-2 and ES14-2008) are statistically identical.

4.2. Geochemistry

A petrographic study of the Essimingor samples indicates that the main phenocryst phase is clinopyroxene with variable amounts of nepheline, titanomagnetite, apatite, perovskite, titanite and minor feldspars and melilite. Sparse groundmass zeolite and calcite indicate some degree of secondary alteration along with iddingsitized olivine found in samples ESMT-6 and ESMT-7 (Appendix A).

The new geochemical data define a SiO_2 undersaturated series from picrite to tephrite to nephelinite to phonolite (Fig. 4) along with a decrease in MgO content from 16.5 to 0.8 wt.% (Fig. 5). The variation of MgO content with other oxides and trace elements defines apparent crystal fractionation paths: Al_2O_3, Na_2O and K_2O correlate negatively with MgO, while CaO correlates positively. The three Essimingor samples from Paslick et al. (1995) are included in Figs. 4, 5, and in isotopic discussions. The major element abundances and isotopic ratios present no indication of interlaboratory bias. The distribution of P_2O_5, TiO_2, and V contents suggest an important role for progressive fractionation of the accessory phases apatite and titanomagnetite at MgO contents less than 8 wt.% (Fig. 5). Many trace elements (Rb, Ba, Sr, Cs, Zr, Hf, Pb, Th) correlate negatively with MgO indicating their incompatibility in the crystallizing assemblage (e.g. Pb in Fig. 5). Other trace elements (e.g. Cr in Fig. 5) correlate positively with MgO and are selectively compatible in key crystallizing phases: Sc, Cr and Ni are compatible in olivine and clinopyroxene, Y is compatible in apatite and perovskite, V is accepted by clinopyroxene and titanomagnetite resulting in a change of slope consistent with the fractionation of the latter, while apatite acts as a sink for REE (e.g. P_2O_5 and La in Fig. 5).

Ce/Pb values display a large range of variation, in the mafic samples (59–22, Fig. 6b). Chondrite normalized REE plots show a preferential enrichment of light REE relative to heavy REE, typical of alkaline magma

Please cite this article as: Mana, S., et al., Geochronology and geochemistry of the Essimingor volcano: Melting of metasomatized lithospheric mantle beneath the North Tanzanian Divergence zone (East African Rift), Lithos (2012), http://dx.doi.org/10.1016/j.lithos.2012.09.009

Table 1
Major (wt.%) and ICP-MS trace element (ppm) results.

Sample	Lab	Locality	SiO_2	TiO_2	Al_2O_3	Fe_2O_3	FeO	FeO_T	MgO	MnO	CaO	Na_2O	K_2O	P_2O_5	V	Cr	Sc	Ni	Cs	Rb	Sr
ES-16	d	S 03° 28' 7.285" E 036° 0' 33.424"	39.9	3.2	6.8	2.32	11.85	14.03	16.5	0.2	13.8	2.6	2.4	0.50	249.3	694.5	26.9	411.5	0.34	51.8	825
ESMT-6	m	S 03° 26' 05.7" E 036° 07' 52.6"	43.78	3.74	8.13	2.12	10.78	13.28	9.84	0.21	17.18	1.72	1.43	0.70	352.33	459.6	–	107	–	32	1175
ESMT-7	m	S 03° 26' 05.6" E 036° 07' 20.0"	42.52	3.88	8.83	2.21	11.27	13.67	9.09	0.22	15.52	3.70	1.78	0.79	360.07	333.43	–	118	–	39	1046
ES-34	d	S 03° 26' 30.684" E 036° 1' 22.239"	37.8	6.1	8.7	2.47	12.58	15.10	7.9	0.3	17.8	2.3	2.0	2.09	511.6	31.5	22.7	57.2	0.48	47.7	1213
ES-21	d	S 03° 27' 49.4" E 036° 00' 52.1"	41.6	4.0	12.2	2.24	11.45	13.40	6.7	0.3	14.2	3.3	3.2	1.05	321.1	52.3	15.9	31.3	0.91	65.4	1919
ES-27	d	S 03° 28' 9.215" E 035° 59' 12.631"	40.6	5.3	11.4	2.27	11.57	13.73	6.4	0.2	14.7	4.2	2.0	1.47	432.6	32.7	18.4	41.3	0.73	50.7	1333
ES10-2008	m	S 03° 25' 42.3" E 036° 03' 08.6"	40.23	5.30	12.00	2.22	11.30	13.98	6.19	0.26	14.39	4.25	2.06	1.36	386.55	12.65	–	33	–	39	1326
ESMT-5	m	S 03° 26' 04.2" E 036° 07' 20.4"	43.79	3.75	13.70	2.05	10.44	12.91	5.46	0.25	11.35	5.41	2.18	1.20	285.31	52.58	–	25	–	101	1283
ESMT-2	m	S 03° 25' 27.7" E 036° 03' 03.3"	40.18	3.46	11.93	1.97	10.07	12.49	4.87	0.33	16.72	5.56	3.06	1.41	402.87	6.41	–	–	–	58	1595
ES17-2008	m	S 03° 26' 07.5" E 036° 07' 29.7"	47.06	3.17	15.64	1.72	8.79	10.77	3.39	0.21	8.69	6.52	3.73	0.83	216.2	6.9	–	–	–	75	1403
ES14-2008	m	S 03° 25' 41.1" E 036° 03' 16.0"	51.26	2.14	17.46	1.33	6.78	8.38	2.48	0.23	6.43	6.66	4.50	0.46	165.61	7.76	–	–	–	127	1927
ESMT-4	m	S 03° 25' 24.9" E 036° 03' 06.9"	51.69	1.81	17.97	1.21	6.16	7.52	1.80	0.22	5.62	8.10	4.90	0.37	143.71	3.69	–	–	–	93	1493
ES-18	d	S 03° 27' 54.0" E 036° 00' 33.1"	54.4	1.3	19.7	1.00	5.09	5.96	1.6	0.2	3.9	8.4	4.2	0.27	86.4	2.3	2.5	3.6	1.17	101.3	1705
ES-6	d	S 03° 28' 0.845" E 035° 59' 47.852"	55.2	1.3	19.6	1.00	5.08	5.97	1.5	0.2	3.8	8.2	3.9	0.29	82.2	3.3	3.1	3.8	1.36	81.6	1706
ES-2	d	S 03° 28' 20.047" E 035° 59' 41.7"	55.0	1.4	19.1	1.03	5.25	6.19	1.3	0.2	4.0	8.1	4.5	0.30	84.1	2.3	2.5	3.2	0.98	103.5	1865
ES-13	d	S 03° 28' 40.796" E 036° 0' 20.436"	54.1	1.5	18.5	1.08	5.53	6.54	1.3	0.2	4.6	8.5	4.3	0.36	100.7	2.2	3.8	3.7	1.35	86.8	1696
ES-8	d	S 03° 27' 53.2" E 035° 59' 40.2"	55.4	1.4	19.2	0.98	4.99	5.95	1.2	0.1	3.9	8.0	4.6	0.28	79.7	2.6	3.9	3.6	0.61	78.1	1652
ES-20	d	S 03° 27' 48.075" E 036° 0' 44.91"	53.6	1.5	18.5	1.07	5.48	6.59	1.2	0.2	4.2	9.7	4.2	0.34	94.9	2.8	3.2	3.8	1.34	93.6	1643
ES-3	d	S 03° 28' 25.0" E 035° 59' 41.7"	55.1	1.4	19.2	1.01	5.14	6.15	1.1	0.1	3.9	8.4	4.2	0.30	82.1	2.6	3.1	3.5	2.11	96.1	1677
ES-7	d	S 03° 28' 0.464" E 035° 59' 45.165"	55.0	1.4	19.0	0.99	5.07	6.09	1.0	0.2	4.2	8.0	4.8	0.30	82.0	2.9	2.6	3.3	1.40	83.7	1755
ES-24	d	S 03° 27' 22.288" E 036° 1' 14.314"	55.1	1.3	19.3	0.99	5.06	5.92	1.0	0.2	4.1	8.5	4.2	0.29	78.3	2.5	3.0	3.7	1.48	105.7	1747
ES-33	d	S 03° 26' 47.953" E 035° 59' 7.165"	56.2	0.9	19.8	0.87	4.46	5.24	0.8	0.2	3.1	8.9	4.6	0.18	57.2	11.6	2.8	6.7	1.69	111.1	1792
Standards																					
W-2	m		52.79	1.06	15.27	10.86	–	–	6.48	0.17	10.9	2.17	0.63	0.13	–	–	–	85	–	19	192
BIR-1	m		47.36	0.95	15.35	11.33	–	–	9.63	0.17	13.2	1.75	0.03	0.03	–	–	–	197	–	0	106
JB-1a	m		–	–	–	–	–	–	–	–	–	–	–	–	203.68	396.8	–	–	–	–	–
RGM-1	d		74.02	0.3	14.3	1.9	–	–	0.30	0.0	1.18	4.2	4.07	0.05	11.91	3.5	5.50	3.45	9.43	144.66	96.15
SDC-1	d		66.73	1.0	16.1	6.8	–	–	1.71	0.1	1.43	2.1	3.59	0.14	93.40	60.2	14.92	33.02	4.11	133.23	181.24
W-2a	d		53.44	1.1	15.7	10.9	–	–	6.41	0.2	10.85	2.3	0.70	0.13	289.43	95.8	38.17	72.01	0.98	21.33	202.90
688.0	d		49.13	1.2	17.7	10.4	–	–	8.62	0.2	12.19	2.1	0.19	0.13	244.23	310.3	36.41	144.19	0.03	2.15	165.11
AII-92	d		58.98	1.0	16.9	6.6	–	–	1.52	0.1	4.89	4.1	2.83	0.17	302.13	231.5	37.61	98.99	0.03	1.39	131.55
AGV-1	d		49.95	1.7	15.3	10.8	–	–	7.48	0.2	11.07	2.9	0.10	0.51	119.50	9.3	11.99	34.18	1.28	69.24	644.75
BIR-1	d		47.94	0.9	15.5	11.4	–	–	9.73	0.2	13.30	1.8	0.08	0.02	310.26	377.5	41.58	164.41	0.00	0.18	104.07
DNC-1	d		47.09	0.5	18.3	9.9	–	–	10.11	0.1	11.13	1.9	0.22	0.06	151.18	285.4	31.33	266.73	0.19	3.82	138.53
G-2	d		67.88	0.5	14.9	2.6	–	–	0.73	0.0	1.93	3.9	4.58	0.1	33.53	7.49	3.27	3.4	1.38	174.53	458.07

m = Michigan State University Laboratory.
d = Duke University Laboratory.

Table 1 (*continued*)

Sample	Ba	Y	Zr	Nb	Hf	Ta	Pb	Th	U	La	Ce	Pr	Nd	Sm	Eu	Gd	Tb	Dy	Ho	Er	Yb	Lu	Zn	Cu
ES-16	598	22.9	207.0	83.5	5.58	5.42	5.23	9.19	1.98	63.1	116.9	14.90	57.84	10.54	2.95	7.41	1.03	5.13	0.88	2.16	1.67	0.21	–	–
ESMT-6	672.12	33.59	317	88.61	8.57	6.14	3.49	10.08	1.67	86.56	151.23	19.5	76.44	13.98	3.76	12.27	1.58	7.12	1.31	3.1	2.54	0.35	101	115
ESMT-7	767.97	36.16	330	96.75	8.92	6.98	3.79	11.16	1.55	96.34	162.84	21.11	82.84	14.79	3.99	13.18	1.71	7.79	1.43	3.32	2.68	0.37	107	179
ES-34	934	56.2	487.2	151.2	12.94	11.94	5.68	21.28	4.15	163.6	329.1	43.02	171.33	30.62	8.80	21.56	2.94	12.44	2.01	4.80	3.70	0.47	–	–
ES-21	736	45.1	464.0	165.6	10.07	9.32	8.56	13.24	3.76	116.4	214.1	26.13	92.09	16.61	4.61	14.53	2.03	9.92	1.70	4.14	3.21	0.41	–	–
ES-27	598	55.0	565.2	189.7	11.94	12.19	11.21	26.66	3.94	179.1	367.4	46.98	171.32	28.80	7.19	23.05	3.04	13.97	2.23	5.17	3.52	0.44	–	–
ES10-2008	512.24	58.34	536	168.49	12.68	13.92	4.92	22.87	3.24	164.28	288.22	37.84	152.25	27.12	7.27	23.48	2.95	12.69	2.28	5.22	4.26	0.55	137	313
ESMT-5	736.88	53.89	525	161.79	12.08	11.14	5.89	17.29	1.76	139.21	234.3	29.25	111.7	19.45	5.28	17.73	2.35	10.65	2.06	4.89	4.22	0.56	136	93
ESMT-2	1251.22	51.77	514	156.18	11.98	5.75	10.03	5.29	2.97	100.39	127.62	14.51	53.37	11.55	3.63	12.19	1.78	9.32	1.85	4.5	3.86	0.53	157	195
ES17-2008	1378.07	49.71	536	174.53	12.63	11.98	9.26	18.24	1.25	156.01	260.16	31.66	117.53	19.93	5.45	18.04	2.29	10.02	1.91	4.67	4.11	0.58	136	58
ES14-2008	1626.04	44.68	502	175	10.41	8.79	12.98	17.99	2.98	123.77	216.46	23.5	82.96	14.51	4.08	13.69	1.82	8	1.58	3.98	3.64	0.5	130	31
ESMT-4	1490.35	40.43	556	175.15	10.73	7.6	17.59	20.98	2.06	117.61	200.14	21.2	72.77	12.62	3.64	12.31	1.62	7.29	1.45	3.79	3.56	0.49	130	42
ES-18	1443	36.7	521.1	148.8	10.26	6.16	22.00	23.94	2.29	117.7	191.7	20.13	65.33	10.43	3.15	8.92	1.36	6.92	1.27	3.35	3.26	0.47	–	–
ES-6	1581	38.8	544.8	162.2	11.03	6.64	23.93	24.92	5.76	120.7	204.5	21.14	67.28	10.88	3.27	9.32	1.41	7.16	1.33	3.60	3.52	0.49	–	–
ES-2	1544	40.4	550.8	161.1	11.21	6.84	16.78	27.10	6.05	125.3	205.7	22.59	74.67	11.74	3.44	9.48	1.40	7.47	1.43	3.95	3.70	0.51	–	–
ES-13	1511	39.9	516.2	157.0	10.83	6.80	21.15	23.40	5.77	121.7	205.5	22.12	74.32	12.15	3.66	9.97	1.45	7.40	1.41	3.77	3.62	0.50	–	–
ES-8	2387	37.2	504.0	149.2	11.07	6.63	23.18	25.12	5.70	108.4	184.8	20.02	69.43	11.27	3.76	8.65	1.28	6.86	1.33	3.75	3.85	0.51	–	–
ES-20	1517	40.7	512.3	153.6	11.16	6.91	18.84	23.42	5.42	121.9	202.9	22.03	73.93	11.84	3.74	9.72	1.45	7.56	1.41	3.84	3.86	0.54	–	–
ES-3	1543	39.9	530.0	157.2	10.97	6.72	23.25	26.60	4.23	120.7	202.7	22.33	75.50	12.06	3.59	9.66	1.43	7.62	1.45	3.97	3.87	0.52	–	–
ES-7	1532	39.2	553.9	162.8	11.02	6.90	23.50	25.20	6.10	122.3	204.1	21.77	71.05	11.38	3.41	9.76	1.46	7.48	1.38	3.63	3.63	0.49	–	–
ES-24	1599	40.6	556.6	161.3	11.74	7.17	22.21	26.79	6.16	128.1	209.0	22.63	74.01	11.74	3.60	9.60	1.42	7.42	1.40	3.83	3.83	0.51	–	–
ES-33	2127	37.6	515.0	147.7	9.99	5.31	28.03	28.82	7.22	122.5	189.7	19.74	64.79	9.73	3.35	7.81	1.20	6.20	1.23	3.43	3.59	0.47	–	–
Standards																								
W-2	–	–	105	–	–	–	–	–	–	–	–	–	–	–	–	–	–	–	–	–	–	–	74	81
BIR-1	–	–	17	–	–	–	–	–	–	–	–	–	–	–	–	–	–	–	–	–	–	–	64	135
JB-1a	490.47	24.41		28.09	3.61	1.83	6.19	9.38	1.63	38.11	64.98	7.18	26.88	5.31	1.53	5.25	0.76	4.11	0.85	2.28	2.21	0.33	–	–
RGM-1	790.59	23.16	223.70	8.86	5.525	0.905	21.146	13.827	5.917	21.94	41.70	5.015	17.199	3.620	0.691	3.492	0.571	3.477	0.713	2.039	2.506	0.376	32.06	10.72
SDC-1	625.36	35.30	41.95	19.07	1.239	1.240	24.342	12.525	3.164	40.17	84.84	11.079	42.837	8.343	1.702	6.842	1.065	6.442	1.304	3.574	3.680	0.490	106.59	35.71
W-2a	181.61	24.37	98.70	7.91	2.573	0.549	7.934	2.291	0.591	11.40	23.51	3.147	12.677	3.200	1.091	3.861	0.679	4.099	0.813	2.173	2.409	0.341	78.82	100.73
688.0	158.69	20.65	55.54	4.24	1.507	0.325	2.328	0.331	0.256	5.12	11.31	1.687	8.361	2.283	0.931	2.869	0.490	3.289	0.731	2.098	2.217	0.328	75.99	84.76
All-92	4.40	39.84	124.20	2.56	3.135	0.566	0.617	0.122	0.109	3.78	12.02	2.229	12.262	4.085	1.349	5.494	0.970	6.631	1.407	4.088	4.328	0.598	92.18	67.15
AGV-1	1262.07	20.78	242.55	14.86	5.187	0.860	37.788	6.896	2.228	39.57	69.12	8.894	32.974	5.959	1.768	4.960	0.712	3.727	0.695	1.878	1.824	0.264	87.91	79.44
BIR-1	5.27	15.64	14.41	0.55	0.570	0.102	2.951	0.007	0.009	0.50	1.74	0.339	2.268	1.084	0.455	1.792	0.333	2.541	0.573	1.635	1.739	0.249	69.45	116.24
DNC-1	100.23	18.20	39.63	1.66	0.981	0.144	5.969	0.256	0.062	3.60	7.84	1.115	5.034	1.384	0.530	1.992	0.373	2.850	0.668	1.890	2.032	0.304	64.60	102.35
G-2	1854.24	9.65	82.80	12.41	1.965	0.782	31.490	25.563	2.341	88.08	160.29	17.21	52.24	7.116	1.714	4.473	0.556	2.196	0.347	0.919	0.719	0.086	81.49	11.1

Table 2
Sample locations and $^{39}Ar/^{40}Ar$ dating results.

Sample ID	Material	Integrated age [Ma]	% Rad	% ^{39}Ar in plateau	Plateau age [Ma]	MSWD	Isochron age of plateau steps [Ma]	$^{40}Ar/^{36}Ar$ intercept	MSWD	Selection criteria
ESMT-6	Matrix	6.97 ± 0.04	18.0		No plateau					II–V
	Whole rock	6.52 ± 0.03	30.2	69.4	6.20 ± 0.03	1.5	5.70 ± 0.40	307 ± 10	0.7	II–V
	Nepheline	16 ± 3	10.1	100.0	15 ± 4	1.6				IV–V
ESMT-7	Matrix	6.24 ± 0.01	74.3	*33.4*	*6.00 ± 0.02*	*1.5*	6.04 ± 0.06	291 ± 6	0.8	II–VI
ES-21	Whole rock	6.11 ± 0.03	55.6		No plateau					II
ES10-2008	Matrix	6.03 ± 0.01	85.3		No plateau					II
	Whole rock	5.70 ± 0.20	72.5		No plateau					II
ESMT-5	Matrix	6.34 ± 0.02	83.2		No plateau					II
	Matrix	6.26 ± 0.02	85.4		No plateau					II
	Nepheline	4.80 ± 0.40	3.0	89.2	6.40 ± 0.30	1.9	7.2 ± 1.2	292 ± 5	1.6	V
ESMT-2	Matrix	5.98 ± 0.01	55.0	79.0	**5.91 ± 0.01**	0.8	**5.91 ± 0.14**	295 ± 12	1.0	I
	Whole rock	5.96 ± 0.01	65.7	53.8	**5.89 ± 0.01**	1.4	**5.85 ± 0.07**	305 ± 15	1.2	I
	Nepheline	6.43 ± 0.01	96.8		No plateau					III
ES17-2008	Matrix	6.24 ± 0.01	89.7		No plateau					II
	Nepheline	16.03 ± 0.17	67.4	*36.6*	*6.10 ± 0.30*	*0.9*	6.58 ± 0.13	282 ± 16	0.4	IV
	Matrix	6.22 ± 0.02	89.2	41.3	6.06 ± 0.03	1.8	6.01 ± 0.17	340 ± 180	2.0	II
ES14-2008	Nepheline	5.83 ± 0.06	85.3	97.4	**5.86 ± 0.07**	1.8	**5.95 ± 0.14**	250 ± 50	1.5	I
	Matrix	5.95 ± 0.01	92.5	50.7	5.90 ± 0.01	2.0	5.81 ± 0.09	410 ± 100	0.1	II
	Matrix (2)	5.91 ± 0.01	93.0	48.0	**5.82 ± 0.02**	2.4	**5.82 ± 0.08**	290 ± 90	2.9	I
	Matrix (2)	5.88 ± 0.01	93.0	*38.4*	*5.74 ± 0.02*	*1.4*	5.76 ± 0.08	280 ± 90	1.6	II
ESMT-4	Nepheline	5.84 ± 0.01	90.7	70.2	**5.87 ± 0.01**	2.1	**5.88 ± 0.03**	282 ± 18	1.7	I
	Matrix	5.92 ± 0.01	89.6		No plateau					II
	Whole rock	5.90 ± 0.01	94.3	*37.1*	*5.77 ± 0.01*	*0.6*	5.77 ± 0.04	310 ± 80	0.9	II
ES-18	Whole rock	5.76 ± 0.02	71.4	58.0	**5.79 ± 0.01**	1.4	**5.82 ± 0.04**	285 ± 14	1.2	I
ES-8	Whole rock	5.90 ± 0.02	84.1	67.9	**5.85 ± 0.02**	0.3	**5.86 ± 0.07**	280 ± 60	0.4	I
ES-3	Whole rock	5.76 ± 0.02	78.4	87.2	**5.76 ± 0.02**	1.6	**5.76 ± 0.04**	297 ± 3	1.6	I

In bold are ages that are considered reliable. The plateau ages errors include error in j. Plateau ages are in good agreement with isochron ages. Plateaus with less than ~40% of the total 39*Ar released are shown in italics. The criteria used in the selection of the analysis are: (I) presence of a plateau, (II) the spectra shows decreasing age with increasing temperature, (III) the spectra are concave shaped, (IV) the spectra are chaotic due to the influence of a secondary component, (V) the analysis gave low % radiogenic argon, and (VI) the plateau is characterized by a low % of the total ^{39}Ar released.

suites (Fig. 7). Primitive mantle-normalized incompatible trace element diagrams of the three most primitive samples (MgO > 9 wt.%) show a pattern comparable to ocean island basalts (Sun and McDonough, 1989) but with much higher concentrations for incompatible trace elements Th, Nb, Ta, La, Ce and Nd. These relatively primitive Essimingor samples also exhibit negative anomalies in Pb, K and P (Fig. 7b). Values of Sr/Ce for the primitive samples (6.4–7.7) fall within the range expected for ocean island basalt (Sun and McDonough, 1989).

The wide variation in radiogenic isotopic ratios at Essimingor (Fig. 8a, b) suggests involvement of at a minimum two components, one of which has elevated Pb isotopic values within the range of HIMU-like samples and a more enriched component (Table 3). Overall the $^{87}Sr/^{86}Sr$ and $^{143}Nd/^{144}Nd$ isotopic ratios are in the middle of the mantle array ($^{87}Sr/^{86}Sr$ 0.703566 to 0.704772 and $^{143}Nd/^{144}Nd$ 0.512473 to 0.512761), whereas the Pb ratios are highly radiogenic with $^{206}Pb/^{204}Pb$ values ranging from 19.6 to 21.3. The $^{207}Pb/^{204}Pb$ values are above the NHRL, whereas $^{208}Pb/^{204}Pb$ values lie on or near the NHRL. The Sr, Nd and Pb isotopic data all correlate well with indices of fractionation, in particular $^{87}Sr/^{86}Sr$ values increase while $^{143}Nd/^{144}Nd$ and $^{206}Pb/^{204}Pb$ decrease consistently with increasing bulk rock SiO_2 (Fig. 9).

5. Discussion

5.1. Timing of Essimingor activity

Laser-incremental heating $^{40}Ar/^{39}Ar$ analyses of whole rock, matrix and nepheline separates of the Essimingor lavas yield plateau ages that range from 5.76 ± 0.02 Ma to 5.91 ± 0.01 Ma. These ages restrict the duration of the Essimingor's volcanism represented by our samples

Table 3
Radiogenic isotope results.

Sample	$^{87}Sr/^{86}Sr$	±2σ	$^{143}Nd/^{144}Nd$	±2σ	$^{206}Pb/^{204}Pb$	±2σ	$^{207}Pb/^{204}Pb$	±2σ	$^{208}Pb/^{204}Pb$	±2σ	Pb method
ES-16	0.703630	0.000006	0.512654	0.000015	21.006	0.001	15.823	0.001	40.676	0.005	p (N = 3)
ESMT-6	0.704326	0.000008	–	–	20.130	0.002	15.742	0.002	40.180	0.005	t
ESMT-7	0.704215	0.000006	0.512657	0.000007	20.127	0.001	15.741	0.001	40.145	0.003	t
ES-34	–	–	0.512716	0.000007	20.782	0.001	15.793	0.000	40.591	0.002	p(N = 2)
ES-21	0.704078	0.000005	0.512722	0.000015	21.150	0.008	15.828	0.006	40.770	0.015	p(N = 3)
ES-27	0.704026	0.000006	0.512745	0.000006	21.299	0.005	15.916	0.004	40.624	0.012	p(N = 3)
ES10-2008	0.703635	0.000006	0.512753	0.000003	21.009	0.002	15.835	0.001	40.713	0.004	t
Same					20.992	0.002	15.798	0.001	40.656	0.003	t
ESMT-5	0.704772	0.000006	0.512622	0.000010	20.050	0.002	15.742	0.001	40.149	0.004	t
ESMT-2	0.703740	0.000006	0.512600	0.000030	21.283	0.004	15.869	0.003	40.653	0.007	t
ES17-2008	0.704722	0.000006	0.512473	0.000014	–	–	–	–	–	–	t
ES14-2008	0.705431	0.000005	0.512434	0.000079	20.303	0.002	15.881	0.002	40.583	0.006	t
ESMT-4	0.705601	0.000008	0.512487	0.000003	20.114	0.005	15.804	0.004	40.587	0.011	t
ES-18	0.705913	0.000008	0.512415	0.000008	19.719	0.004	15.778	0.003	40.529	0.008	p(N = 3)
ES-8	0.706217	0.000008	0.512407	0.000003	19.635	0.002	15.774	0.002	40.534	0.007	p(N = 3)
ES-3	0.706241	0.000011	–	–	19.624	0.003	15.773	0.002	40.546	0.007	p(N = 3)
NIST 981					16.94142	0.00317	15.49661	0.00305	36.70262	0.00827	p(N = 20)

Pb method: t = TIMS; p = Fisons Plasma 54 (MC-MS-ICPMS).

Please cite this article as: Mana, S., et al., Geochronology and geochemistry of the Essimingor volcano: Melting of metasomatized lithospheric mantle beneath the North Tanzanian Divergence zone (East African Rift), Lithos (2012), http://dx.doi.org/10.1016/j.lithos.2012.09.009

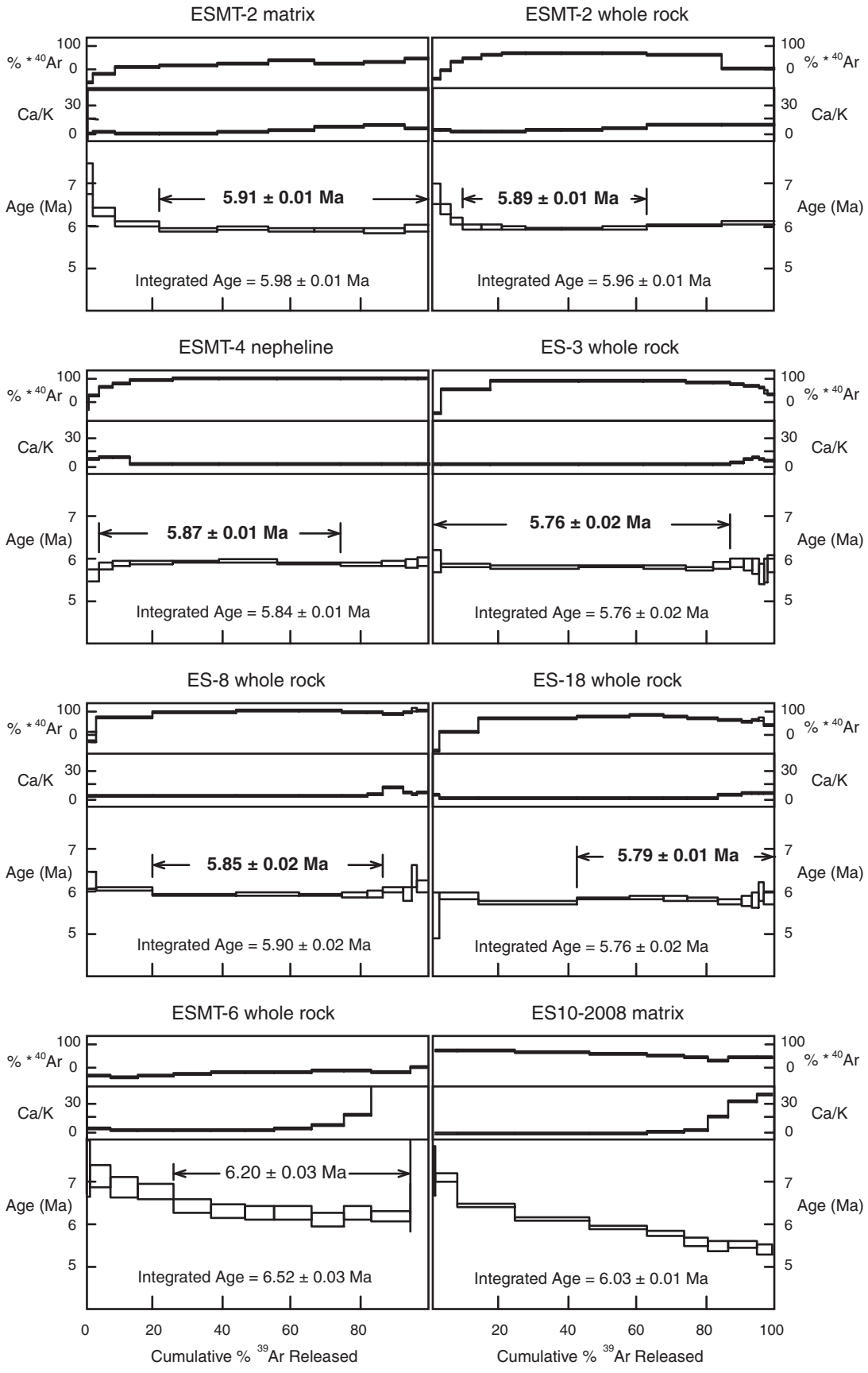

Fig. 2. $^{40}Ar/^{39}Ar$ incremental-heating spectra. The plateau ages are weighted averages of the individual plateau steps. Errors are 2σ confidence level. Steps included in the plateaus are bracketed by arrows. Based on the selection criteria of Table 2 the top six plots are preferred ages, whereas the bottom two are examples of the rejected criteria.

Please cite this article as: Mana, S., et al., Geochronology and geochemistry of the Essimingor volcano: Melting of metasomatized lithospheric mantle beneath the North Tanzanian Divergence zone (East African Rift), Lithos (2012), http://dx.doi.org/10.1016/j.lithos.2012.09.009

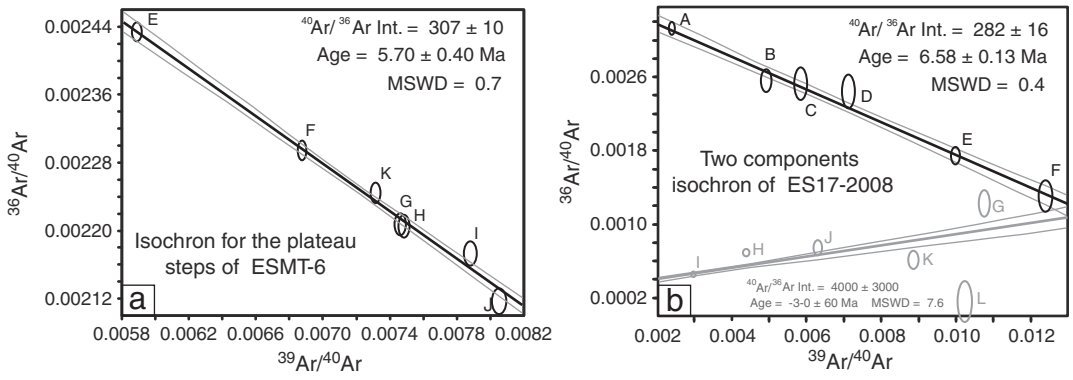

Fig. 3. Inverse isochron plots. (a) Data for ESMT-6 whole rock are well behaved with little scattering along a line fit (MSWD = 0.7) and ^{40}Ar/^{36}Ar intercept is indistinguishable from atmospheric ratios (^{40}Ar/^{36}Ar Int.); (b) Data for ES17-2008 nepheline reveals two components.

to approximately 150 ± 20 kyr. Our ^{40}Ar/^{39}Ar ages are roughly 2 myr younger than K–Ar ages previously reported by Bagdasaryan et al. (1973). It is unclear if this difference in age is due to limitations of the K–Ar method or if the K–Ar ages were obtained from flows unsampled by our team; the location from which the Bagdasaryan samples were collected is unknown and therefore not re-testable. Nevertheless, due to accessibility reasons the sample is most likely from the same area. Nepheline separates from some of our dated samples give anomalous integrated (K–Ar equivalent) ages as old as 16 Ma (Table 2). We interpret the old ages of Bagdasaryan samples as possibly reflecting excess or trapped Ar in nepheline incorporated in the whole rock samples.

5.2. Source mineralogy and depth of melting

Xenolith studies from the NTD indicate the presence of a metasomatized lithospheric mantle beneath the area (e.g. Aulbach et al., 2011; Dawson and Smith, 1988, 1992; Pike et al., 1980; Rudnick et al., 1993). The study of incompatible trace elements is here used to estimate the mineralogy of the melting source giving useful constraints on the mantle's thermal characteristics and metasomatic history. To mitigate the effects of fractionation and assimilation on trace element abundances we focus our discussion on the most primitive samples that contain >9 wt.% MgO (Fig. 7b). The negative Pb anomaly of Essimingor's more primitive samples in conjunction with Sr/Ce values within the range expected for oceanic basalt confirm their lack of significant crustal assimilation, assuming an upper continental crust of overall granitic composition. Primitive mantle-normalized REE variations from Tb to Lu are steep to concave upward (Fig. 7b). This pattern suggests the presence of a residual mineral phase in which these elements are compatible, e.g. garnet. Potassium depletion correlated with Ba enrichment and slight Rb depletion, that manifests as Ba/Rb > 11 (Sun and McDonough, 1989), implies the presence of amphibole in the source (Adam et al., 1993; LaTourette et al., 1995). Low Rb and Cs abundances with high Ba contents have been explained in other alkaline rocks as indicating the presence of phlogopite in the source (Foley and Jenner, 2004; Platz et al., 2004). Xenoliths containing both amphibole and phlogopite from northern Tanzania (Dawson and Smith, 1988, 1992) support the presence of both of these phases in the source region. The observed anomalously high Zr/Hf values (37–52) at Essimingor are a characteristic signature of carbonatite metasomatism (Dupuy et al., 1992; Rudnick et al., 1993). In summary, the trace elements of the most primitive samples indicate partial melting of a metasomatized lithospheric mantle that includes garnet, phlogopite and small amounts of amphibole. The coexistence of garnet and phlogopite in the source suggests depth of melting from ~80 km up to ~150 km (Foley, 1993; Olafsson and Eggler, 1983; Sato et al., 1997), consistent with the base of the lithosphere in the eastern branch identified using Rayleigh wave tomography (120–160 km; Weeraratne et al., 2003) and indicating that Essimingor represents the initial phase of lithospheric thinning through melting.

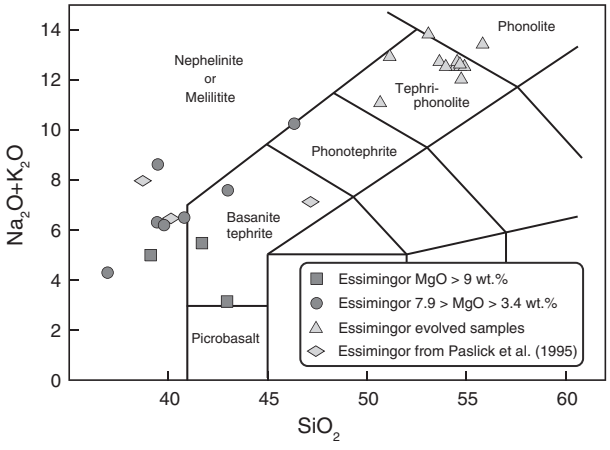

Fig. 4. Total alkali versus silica diagram (Le Maitre et al., 1989) for Essimingor lavas. Major element values are reported in wt.%.

5.3. Effects of crustal assimilation

Open system processes are required from the observed increase in Sr, Nd, and Pb isotopic values with indices of fractionation (Fig. 9). Although the major elements show well-defined trends, fractional crystallization alone cannot explain the broad variation of some incompatible trace elements. Ce/Pb has a large variation (Fig. 6b) and samples with low Ce/Pb values have high Pb contents, which imply crustal assimilation overprinting the mantle signature (Hofmann et al., 1986; Sun and McDonough, 1989). In a primitive-mantle normalized incompatible trace element diagram (Fig. 7c), Pb shows a positive anomaly for samples with low MgO content and the higher Pb abundances correspond to low Ce/Pb values (Fig. 6b) consistent with crustal assimilation. Other elements such as U, Th and Cs, which are both fluid-mobile and generally highly abundant in the shallow crust, display negative correlation.

5.4. Source modeling: partial melting and AFC

Isotopes and rare earth elements present clear systematics, which underline the presence of slightly different degrees of partial melting, source heterogeneity and AFC processes. Quantitative models were calculated using IGPET petrologic software (Terra Softa Inc.). The partition coefficients used are from the GERM website (Geochemical Earth Reference Model). We model Essimingor's mantle source mineralogy by

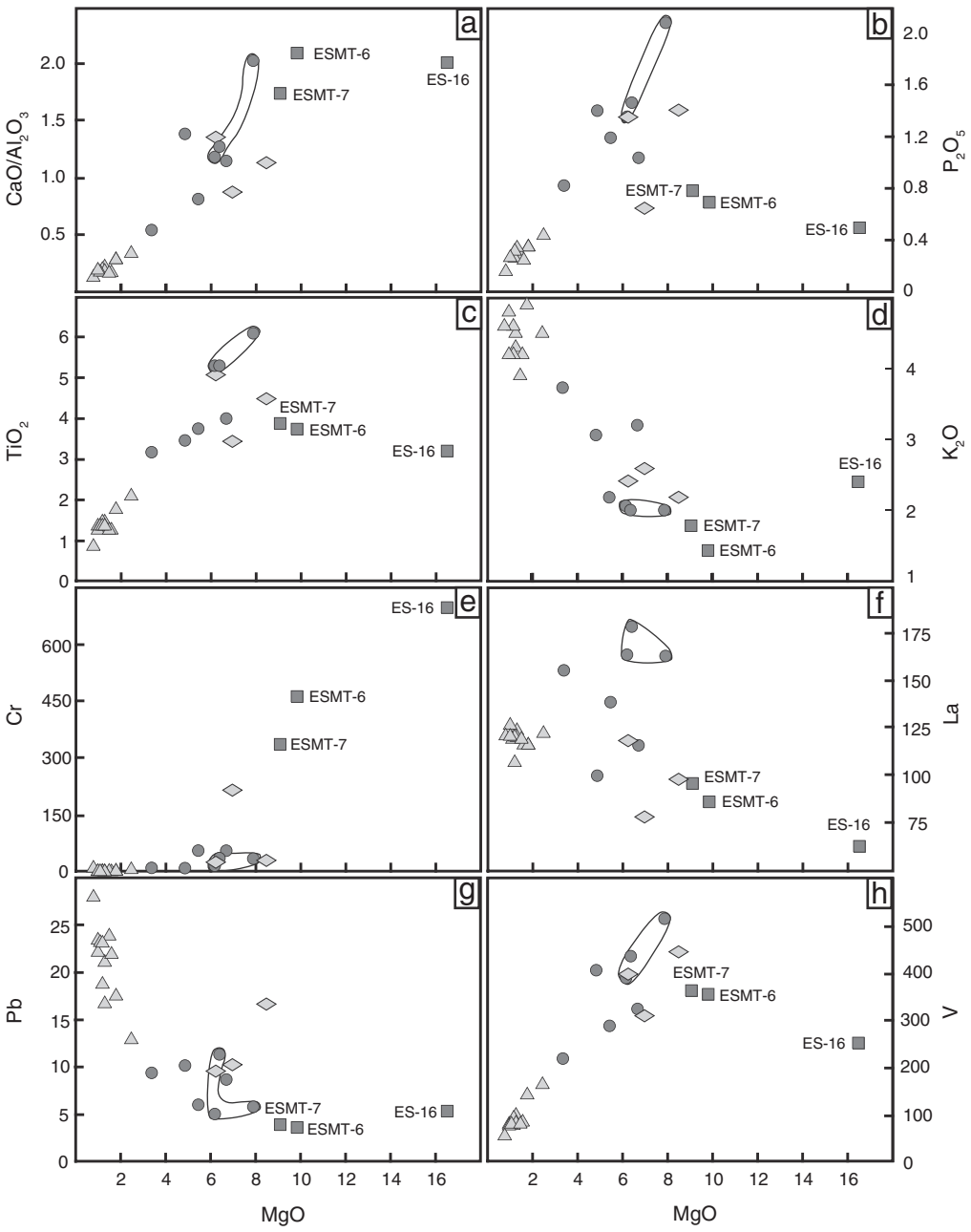

Fig. 5. (a, b, c, d, e, f, h) Major element variations of Essimingor lavas show trends that suggest fractional crystallization. (g) Pb versus MgO suggests the presence of assimilation. Symbols as in Fig. 4; major elements values are reported in wt.%, while trace elements in this and following plots are in ppm. The three circled samples are distinct by being enriched in various rare earth elements.

back-calculating under the assumption that OIB-like magmas, similar in trace elements composition to Essimingor basalts (Fig. 7b) form by melting 5% of a source composed of 20% clinopyroxene, 20% orthopyroxene and 60% olivine. Partial melting of this modeled mantle with additional minor garnet, phlogopite and amphibole have been modeled in Fig. 6c (olivine 60%, clinopyroxene 16%, orthopyroxene 16%, phlogopite 5%, amphibole 2% and garnet 1%, with increasing garnet (up to 3%) compensated by a reduction in modal olivine). In this plot La/Sm variations indicate different degrees of partial melting, and increasing Sm/Y values reflect increasing amounts of garnet in the source. Note that small variations in the garnet content can explain the range of plausible parental compositions observed at Essimingor with degrees of partial melting between 2 and 3%.

A quantitative model of the proposed crustal assimilation was attempted after a survey of various modeled crustal compositions (Rudnick and Fountain, 1995; Rudnick and Gao, 2003; Shaw et al., 1986; Taylor and McLennan, 1985, 1995) and EAR local possible contaminants (e.g. Bell and Simonetti, 1996; Bell and Tilton, 2001; Cloutier et al., 2005; De Mulder, 1985; Kalt et al., 1997; Mansur, 2008; Manya et al., 2007). The large increase in Sr isotope ratios for the evolved samples (Fig. 6a) indicates that the contaminant has very radiogenic Sr isotope values, typical of an upper crustal component (Rollinson, 1993). Any AFC model is an approximation, but this is even more true in the presence of a complex tectonic setting such as the one of North Tanzania, resulting in a crust that can be heterogeneous at all depths. We selected a crustal sample that appears to better describe the major and trace element features of a possible contaminant as it provides a reasonable fit to the observed data. Sample TA-47 has been described as a Na-rich granitoid; it is from the Musoma–Mara Greenstone Belt, northern Tanzania (Manya et al.,

Please cite this article as: Mana, S., et al., Geochronology and geochemistry of the Essimingor volcano: Melting of metasomatized lithospheric mantle beneath the North Tanzanian Divergence zone (East African Rift), Lithos (2012), http://dx.doi.org/10.1016/j.lithos.2012.09.009

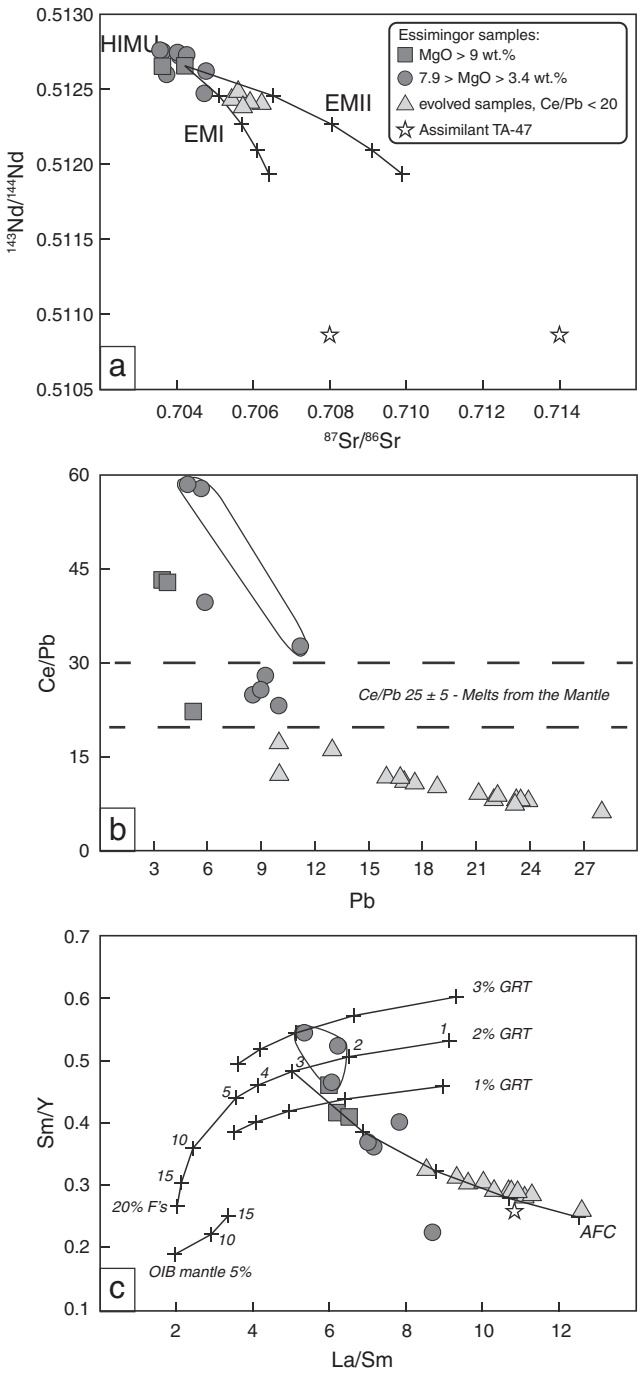

Fig. 6. (a) AFC model for $^{87}Sr/^{86}Sr$ and $^{143}Nd/^{144}Nd$. $^{87}Sr/^{86}Sr$ was not determined for sample TA-47, so a range of possible values is hypothesized here. (b) Pb versus Ce/Pb supports the presence of crustal assimilation (Hofmann et al., 1986; Sun and McDonough, 1989). (c) La/Sm versus Sm/Y illustrating our partial melting model and AFC trend. Partial melting was modeled based on the following mineral phase mode: olivine 60%, clinopyroxene 16%, orthopyroxene 16%, phlogopite 5%, amphibole 2% and garnet 1% (with garnet variation balanced by the olivine content at 1, 2 and 3%). AFC mode was calculated as: clinopyroxene 63%, nepheline 21%, magnetite 14%, apatite 1%, perovskite 0.5% and sphene 0.5%. F steps in the AFC model are 5%. The three circled samples can be explained by melting a source slightly more enriched in garnet (see text for details).

2007), and forms part of the Tanzanian Craton. We performed AFC modeling with the assimilation of sample TA-47, and found that the best fit was obtained using a ratio R_a (mass assimilated divided by mass crystallized; DePaolo, 1981) of 1.1. Sample TA-47 does not have an $^{87}Sr/^{86}Sr$ isotope value so we introduced two hypothetical values creating a range of possibilities. The $^{87}Sr/^{86}Sr$ versus $^{143}Nd/^{144}Nd$ isotopes plot (Fig. 6a) shows a good fit for $^{87}Sr/^{86}Sr$ values ranging between 0.708 and 0.714.

Our AFC model fits the REE other than Yb and Lu quite well (Fig. 6c). The LILE and the HFSE (not shown) are also fit by this model, other than for Zr and Nb that present a misfit. These poor fits are a reminder that the "best" crustal xenolith has not yet been found, or that no single sample can represent the complex process of crustal assimilation observed, although its composition is generally well described by the sample selected. Note that three samples (ES10-2008, ES-27, ES-34) are distinct by being enriched in various rare earth elements resulting in, for example, anomalously high Ce/Pb values (Fig. 6b). These samples, grouped in Figs. 5 and 6, can be explained by melting a source that is slightly more enriched in garnet.

Shallow fractional crystallization affects the major element behavior at Essimingor. The main mineral phase fractionating at Essimingor during the early stages is clinopyroxene rather than olivine. This observation is consistent with the major element compositions of Essimingor samples compared to experimentally-derived alkalic liquids over a range of pressures from 1 atm to 20 kbar (Sack et al., 1987). Based on the work of Albarède et al. (1997) and O'Hara (1968), clinopyroxene dominates the fractionation at high pressure, with stability crossover between olivine and clinopyroxene at 9 ± 2 kbar. Based on petrography, at Essimingor the liquidus mineral is clinopyroxene, hence mineral fractionation is happening at ~25 km depth (Albarède et al., 1997).

5.5. Mixing of two distinct lithospheric mantle sources

The silica-undersaturated lavas from Essimingor are derived from melting of a lithospheric mantle containing garnet, phlogopite and minor amounts of amphibole that were added by one or more events of metasomatism. There is a general good agreement between the trace element abundance pattern observed at Essimingor and those observed in portions of the western branch of the East African Rift (Toro Ankole; Fig. 7b). At Essimingor, variations in $^{143}Nd/^{144}Nd$ against key incompatible trace element ratios (e.g. Th/Nb, Zr/Hf) somewhat overlap the field of regional convergence described by Furman and Graham (1999) as a common lithospheric mantle. However, the lithospheric mantle defined by Essimingor is isotopically distinct in $^{207}Pb/^{204}Pb$ (not shown) and $^{208}Pb/^{204}Pb$ space (Fig. 8b) from the one observed in the western branch of the EAR (Toro Ankole; Davies and Lloyd, 1989; Virunga; Rogers et al., 1992, 1998). Virunga and Toro Ankole are indicative of melts derived from an ancient metasomatized lithosphere. Essimingor samples may represent melting of a different (and in this case, younger) lithosphere consistent with the distribution of the Proterozoic Mozambique Belt (Macdonald et al., 1995, 2001; Möller et al., 1998; Rogers et al., 2000). The presence of a cluster of Essimingor samples which trend towards lower $^{206}Pb/^{204}Pb$ values may represent evidence of material contribution from both of these two lithospheres (Fig. 8b), while evolved lavas appear to indicate additional incorporation of granitic crustal material during AFC processes. The NTD and Essimingor volcano are located at a fundamental tectonic boundary between the Tanzanian Craton and the Mozambique Belt (Smith, 1994), and the Pb isotopic compositions of Essimingor basalts appear to record an area in which rising magmas are sampling multiple lithospheres. These isotopic results agree with the model from Fritz et al. (2009) who proposed that the Proterozoic Mozambique Belt is thrust westward over the Archean Tanzanian Craton.

5.6. Origin of metasomatism

Isotopic compositions of peridotite xenoliths in Tanzania are interpreted as the result of a variable degree of metasomatism by silicate and/or carbonatite melts (e.g. Aulbach et al., 2008, 2011;

Please cite this article as: Mana, S., et al., Geochronology and geochemistry of the Essimingor volcano: Melting of metasomatized lithospheric mantle beneath the North Tanzanian Divergence zone (East African Rift), Lithos (2012), http://dx.doi.org/10.1016/j.lithos.2012.09.009

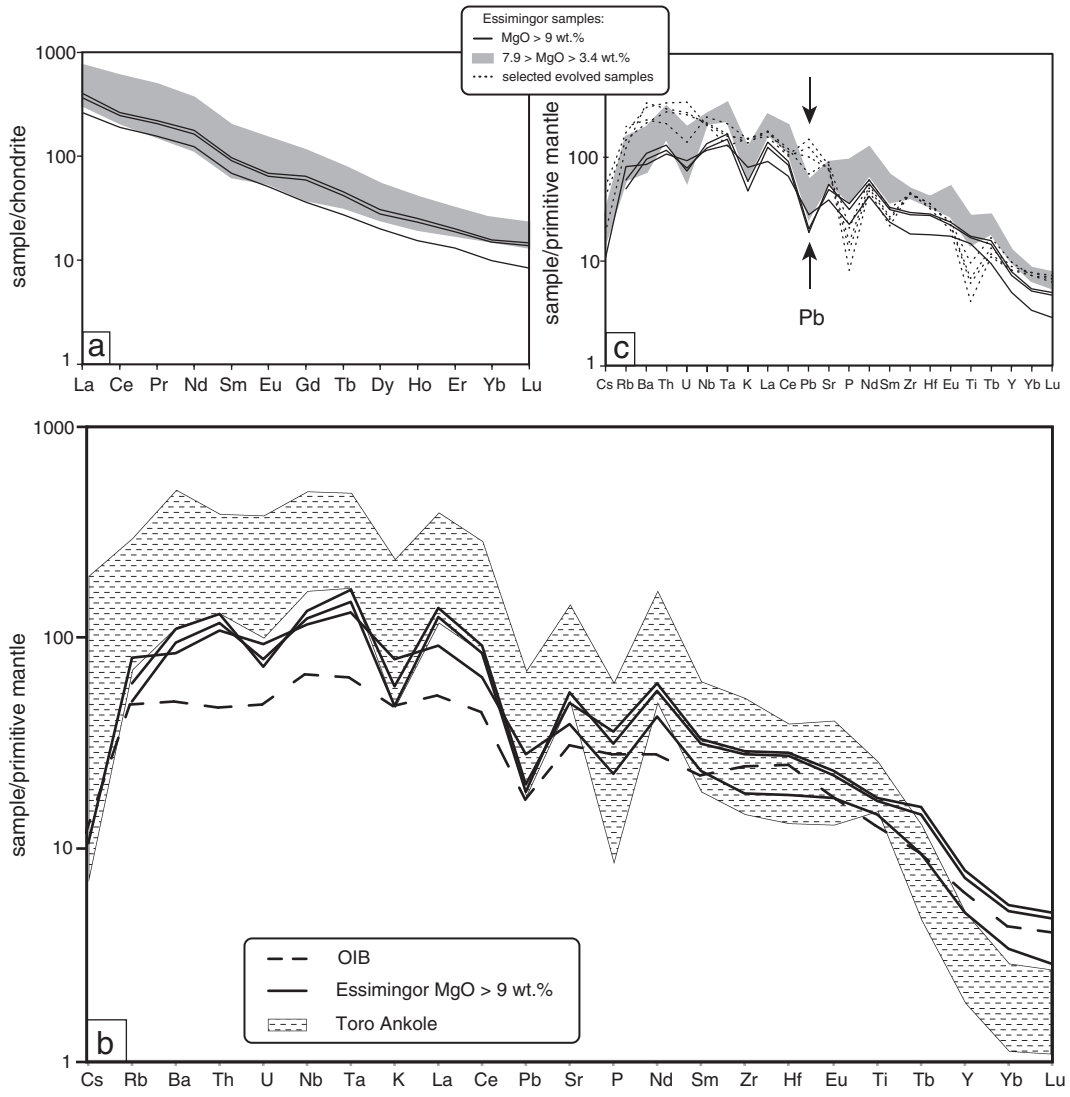

Fig. 7. (a) Chondrite normalized incompatible element variation diagram (normalization values from Sun and McDonough, 1989). (b) Primitive mantle normalized incompatible element variation diagram for mafic rift volcanics (normalization values from Sun and McDonough, 1989). (c) Primitive mantle normalized incompatible element variation diagram for Essimingor samples. Dashed lines represent the distribution of selected evolved samples characterized by Ce/Pb<20, notice their enrichment in Pb.
Sources of data for panel b: Toro Ankole (includes only samples with MgO>6 wt.%) — Rosenthal et al. (2009); OIB — Sun and McDonough (1989).

Chesley et al., 1999; Cohen et al., 1984; Dawson and Smith, 1988, 1992; Lee and Rudnick, 1999; Lloyd et al., 1985; Pike et al., 1980; Rudnick et al., 1993). Aulbach et al. (2011) underlined evidence for the presence of more than one episode of mantle modification. One event was associated to the recent rift-related intrusion of sublithospheric melts and fluids already identified by Rudnick et al. (1993). Based on the similarity between the isotopic signature of the xenoliths and young primitive east African carbonatites and basalts this metasomatism occurred recently. In contrast, other episodes of metasomatism are older and characterized consistently by higher $^{87}Sr/^{86}Sr$ values and lower $^{143}Nd/^{144}Nd$ values. The Essimingor isotopes broadly parallel with the East African carbonatite distribution that Bell and Simonetti (2010) interpret as related to the recent volcanism. The range of variation of Sr and Nd isotopes at Essimingor are wide and define a field much larger than the range defined by Oldoinyo Lengai (Fig. 8a), and consistent with the distribution of peridotite xenoliths from Lashaine and Labait that the authors interpret as ancient enriched lithospheric (Aulbach et al., 2011; Fig. 8a except few outliers extending towards higher $^{87}Sr/^{86}Sr$ values). This study cannot provide a constraint on the timing of metasomatism, however, based on the identification of our source as a metasomatized lithospheric mantle with a HIMU-like signature and the absence of a clear overlap between the Essimingor samples and the modeled plume, we choose to interpret the observed metasomatism as ancient metasomatism, unrelated to the modern impinging of the plume.

5.7. NTD temporal isotopic variations

Integration of the various available NTD isotopic data underlines the presence of wide Pb variations that, being inconsistent with spatial distribution, we interpret as temporal (Fig. 10a and b). The older NTD mafic extrusives (5.9 to 3 Ma) have distinctly more radiogenic Pb isotopic compositions than samples from the younger volcanism (2.5 Ma to Present) (Fig. 10b). The variations in $^{87}Sr/^{86}Sr$ and $^{143}Nd/^{144}Nd$ appear not to be time dependent, although the younger extrusives extend further towards enriched mantle components (Fig. 10a). The older extrusives have Sr–Nd–Pb isotopic compositions that plot consistently close to HIMU-like values (even before being filtered for MgO>6 wt.% and 20<Ce/Pb<30, Fig. 10b), whereas in Pb space younger mafic volcanics approach the Afar plume composition (Furman et al., 2006a and references therein) and extend towards lower Pb values. It is unlikely that the Afar plume extends as far south as the NTD. The Kenya plume

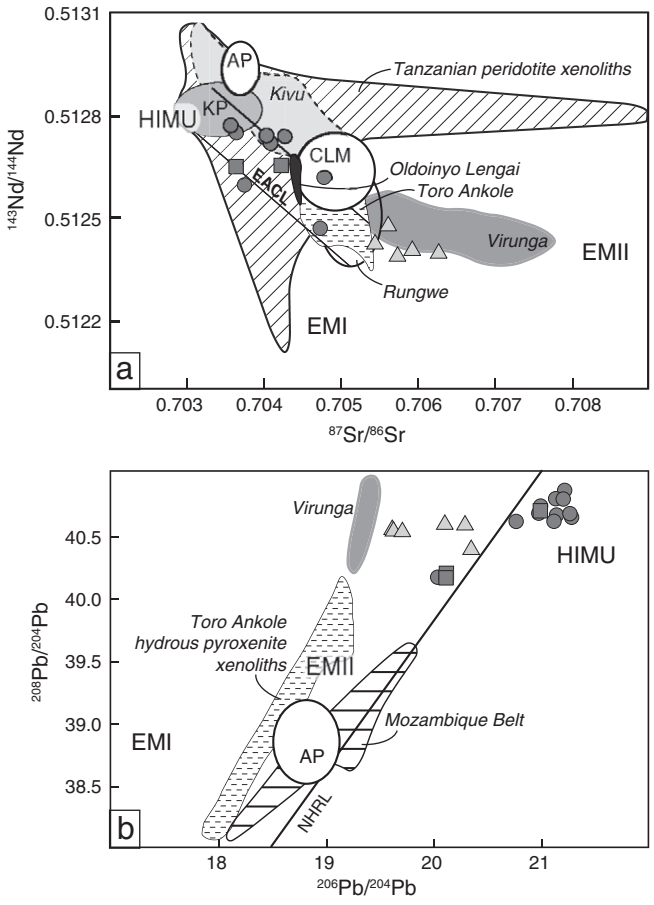

Fig. 8. Isotope variation diagrams comparing Essimingor data to fields of published regional sample sets (all regional samples have MgO > 6 wt.%). Symbols as in previous figures. Isotopic ratios for mantle end-members from literature (when more than one reference is reported the average has been used): EM1 (Hart et al., 1992; Jackson and Dasgupta, 2008; Zindler and Hart, 1986); EM2 (Hart et al., 1992; Jackson and Dasgupta, 2008; Workman et al., 2004; Zindler and Hart, 1986); HIMU (Hart et al., 1992; Jackson and Dasgupta, 2008; Zindler and Hart, 1986). AP = Afar plume (Furman et al., 2006a and references therein), KP = Kenya plume (Aulbach et al., 2011) and CLM = Common Lithospheric Mantle (Furman and Graham, 1999). (a) $^{87}Sr/^{86}Sr$ versus $^{143}Nd/^{144}Nd$. For comparison we report various Western Rift magmatic provinces. (b) $^{206}Pb/^{204}Pb$ versus $^{208}Pb/^{204}Pb$. Essimingor samples lay on the Mozambique Belt alignment. Field of variation from: Macdonald et al. (1995, 2001); Möller et al. (1998); Rogers et al. (2000). Toro Ankole hydrous pyroxenite xenoliths from Davies and Lloyd (1989) and magmas from Virunga define a second field that is interpreted as recording melting of ancient metasomatized lithospheric mantle. A small group of Essimingor samples plot between these two groups, and may record contributions from both of these two sources. Northern Hemisphere Reference Line (NHRL) from Hart (1984).
Sources of data for panel a: Kivu; Furman and Graham (1999); Virunga; Rogers et al. (1992, 1998); Toro Ankole; Rosenthal et al. (2009); Rungwe; Furman (1995). The Tanzanian peridotite xenoliths field is from Aulbach et al. (2011) including xenoliths from Lashaine, Labait and Olmani/Pello Hill, except few outliers, which plot at much higher $^{87}Sr/^{86}Sr$ values. East African carbonatite line (EACL) and Oldoinyo Lengai range are from Bell and Simonetti (2010).

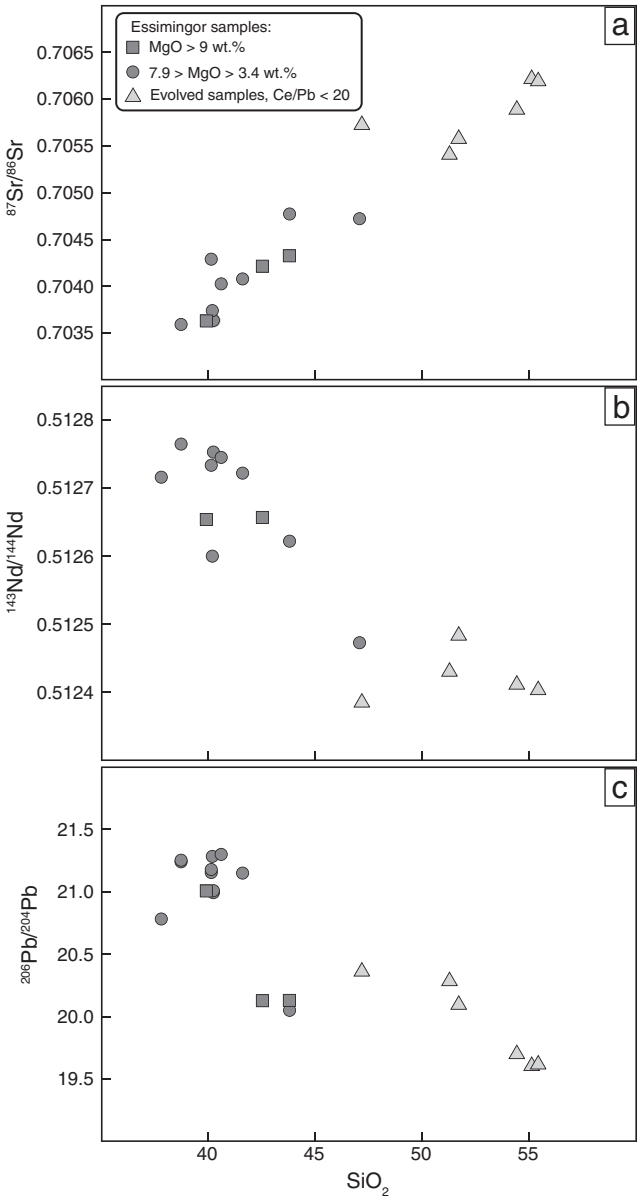

Fig. 9. SiO_2 (wt.%) versus $^{87}Sr/^{86}Sr$, $^{143}Nd/^{144}Nd$ and $^{206}Pb/^{204}Pb$ ratios for all Essimingor samples. The large correlated variations are consistent with crustal assimilation.

is closer geographically and in Sr–Nd space. Unfortunately, the Pb isotopic signature of the Kenya plume has not been established. The apparent time dependence in the Pb isotopic signatures is intriguing and underlines the necessity of further isotopic studies in order to make a clearer dynamic model of the area. On the basis of these limited data, we suggest that the oldest NTD lavas, with isotopic compositions consistent with the involvement of a HIMU-like source, might be derived from the melting of sub-continental lithospheric mantle caused by heat transfer from an impinging plume head, while younger NTD lavas reflect greater stages of lithospheric removal and higher contributions from a plume-like component.

6. Summary

Laser-incremental heating $^{40}Ar/^{39}Ar$ analyses of the Essimingor lavas yield plateau ages that range from 5.76 ± 0.02 Ma to 5.91 ± 0.01 Ma, about 2 myr younger than K–Ar ages of ~8 Ma previously reported. These younger ages underline the importance of $^{40}Ar/^{39}Ar$ studies of rift volcanoes in order to achieve a more detailed rift evolution understanding. Nonetheless, our new $^{40}Ar/^{39}Ar$ ages support the widespread interpretation of Essimingor as the oldest NTD volcano.

Essimingor erupted undersaturated lavas evolving from picrite to tephrite, nephelinite and tephri-phonolite. The major elements suggest an influence of fractional crystallization while the isotopic and incompatible trace element variations demand open system processes involving the assimilation of granitic crust. For the most primitive lavas,

Please cite this article as: Mana, S., et al., Geochronology and geochemistry of the Essimingor volcano: Melting of metasomatized lithospheric mantle beneath the North Tanzanian Divergence zone (East African Rift), Lithos (2012), http://dx.doi.org/10.1016/j.lithos.2012.09.009

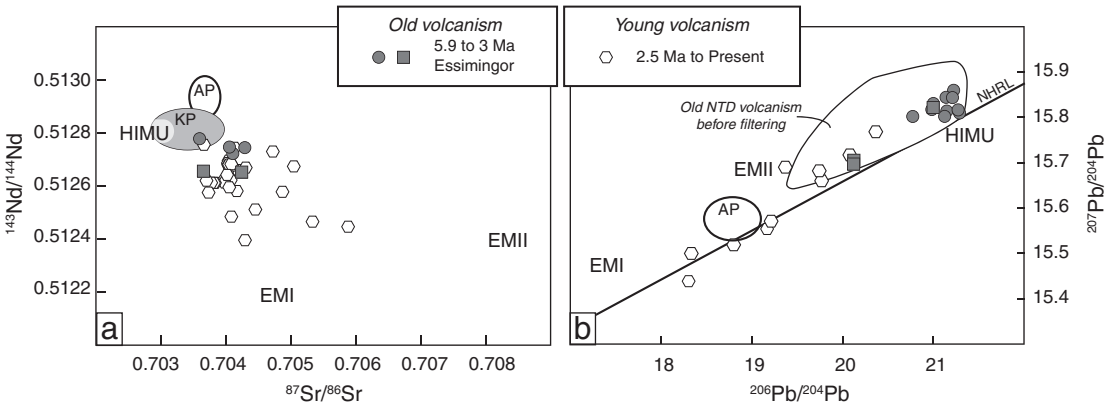

Fig. 10. (a) $^{87}Sr/^{86}Sr$ versus $^{143}Nd/^{144}Nd$ and (d) $^{206}Pb/^{204}Pb$ versus $^{207}Pb/^{204}Pb$ for mafic rocks of the North Tanzanian Divergence zone. Only samples with 20<Ce/Pb<30 and MgO>6 wt.% are plotted. Older extrusive=5.9 to 3 Ma (Essimingor, Satiman, Engelosin; Paslick et al., 1995; Mollel et al., 2008, 2009, 2011; this work); younger extrusives=2.5 Ma to Present (Lemagrut, Ogol, Ngorongoro, Olmoti, Oldeani, Loolmalasin, Embagai, Ketumbeine, Tarosero, Burko, Monduli, Shira, Kerimasi, Meru, Kibo, Mawenzi; Evans et al., 1971; Downie and Wilkinson, 1972; Fairhead et al., 1972; Isaacs and Curtis, 1974; MacIntyre et al., 1974; Hay, 1976; Wilkinson et al., 1986; Paslick et al., 1995; Kalt et al., 1997; Hayes, 2004; Mollel et al., 2008, 2009, 2011; Nonnotte et al., 2008, 2011). The field in plot (b) represents the distribution of isotopic characteristics of the older volcanics before removing samples that do not meet our geochemical criteria.

trace element variations are consistent with melting a metasomatized source with residual garnet, phlogopite, and minor amphibole. This process can be modeled successfully with low degrees of partial melting (<4%) of a source characterized by a slightly variable garnet content. High $(La/Yb)_n$ values and REE abundances in Essimingor mafic lavas are consistent with melting in the garnet and phlogopite stability zone indicating the presence of a relatively thick lithosphere. Essimingor represents the beginning of a process of lithospheric removal by melting during extension. The Pb isotopic distribution at Essimingor is indicative of contributions from two distinct lithospheric mantles caused by the location of the NTD at a fundamental tectonic boundary between the Archean Tanzanian Craton and the Proterozoic Mozambique Belt.

Acknowledgments

This work was supported by Rutgers University School of Arts and Sciences to Swisher and the Alliance for Earth Science, Engineering and Development in Africa at the Pennsylvania State University, and an NSF grant OISE 0827211 to Furman. We are grateful to Gary Dwyer at Duke University for the bulk geochemical analyses of Essimingor samples and to Jeremy Delaney for the Microprobe data. Many thanks to J. B. Dawson for providing the GPS locations of samples reported in Paslick et al. (1995). We thank Sonja Aulbach and an anonymous reviewer for constructive comments that helped clarify our ideas.

Appendix A

Sample code	Microscopic description
ES-2	Fluidal glomeroporphyritic texture. Matrix (85%) glassy with feldspar and pyroxene microlites. Phenocrysts: pleocroic zonated clinopyroxene (9%) up to 3 mm long, titanite (3%) up to 2 mm long, opaque (2%), and melilite (1%).
ES-3	Fluidal glomeroporphyritic texture. Matrix (85%) glassy with feldspar and pyroxene microlites. Phenocrysts: green and beige pleocroic zonated clinopyroxene (8%) up to 3 mm long, titanite (4%) up to 1.8 mm long, opaque (2%), and melilite (1%).
ES-6	Fluidal porphyritic texture with some mineral cluster. Matrix (80%) glassy with feldspar and pyroxene microlites. Phenocrysts: green pleocroic zonated clinopyroxene (12%) up to 3.5 mm long, titanite (4%) up to 1 mm long, opaque (2%), nepheline (1%), melilite (1%) and sparse apatite. Presence of sparce zeolite.
ES-7	Porphyritic texture with some mineral cluster. Matrix (80%) glassy with feldspar and pyroxene microlites. Phenocrysts: green pleocroic zonated clinopyroxene (12%) up to 5 mm long, titanite (3.5%) up to ~1 mm long, nepheline (2%), opaque (1.5%), and melilite (1%). Presence of sparce zeolite. Presence of autholiths (CPX + opaque + neph + sphene).
ES-8	Fluidal porphyritic texture with sparse mineral cluster. Matrix (85%) glassy with feldspar, nepheline and pyroxene microlites. Phenocrysts: clinopyroxene (8%) up to 2.5 mm long, titanite (3%) up to ~2 mm long, opaque (2%), nepheline (1%), and melilite (1%). Presence of autholiths (CPX + opaque + neph).
ES-13	Fluidal seriated porphyritic texture. Matrix (85%) glassy with feldspar, pyroxene, nepheline and sphene microlites. Phenocrysts: clinopyroxene (8%) up to 1.5 mm long, sphene (2%), opaque (2%), nepheline (2%), melilite (1%). Presence of autholiths (CPX + opaque + neph).
ES-16	Fluidal porphyritic texture. Matrix (90%) glassy with melilite, pyroxene, nepheline and sphene microlites. Phenocrysts: clinopyroxene (6%) up to 2.5 mm long, titanite (1.5%), nepheline (1.5%), and opaque (1%). Presence of autholiths (CPX + opaque + sphene).
ES-18	Porphyritic texture. Matrix (80%) glassy with nepheline, feldspar and pyroxene microlites. Phenocrysts: clinopyroxene (13%) up to 2 mm long, nepheline (3%), titanite (2%), opaque (1%), and apatite (1%). Presence of autholiths (CPX + opaque).
ES-20	Glomeroporphyritic texture. Matrix (90%) glassy with feldspar and pyroxene microlites. Phenocrysts: clinopyroxene (6%) up to 2 mm long, titanite (2%), nepheline (1%), and opaque (1%). Presence of autholiths (CPX + opaque + sphene).
ES-21	Porphyritic texture. Matrix (50%) microcrystalline with mainly nepheline, opaque and pyroxene microlites. Phenocrysts: beige zonated, non pleocroic clinopyroxene (35%) up to 4×2 mm, opaque (4%) and nepheline (1%). Presence of calcite xenocrysts with leucite inclusion (10%).
ES-24	Fluidal porphyritic texture. Matrix (90%) glassy with feldspar, pyroxene, opaque and sphene microlites. Phenocrysts: clinopyroxene (6%) up to 4×1 mm, opaque (2.5%), and titanite (1.5%).
ES-27	Porphyritic texture. Matrix (60%) glassy with pyroxene and opaque microlites. Phenocrysts: beige clinopyroxene (32%) up to 5×1 mm, opaque (4%), apatite (2%) up to 0.5 mm, and perovskite (2%).
ES-33	Fluidal porphyritic texture. Matrix (90%) glassy with melilite, pyroxene and titanite microlites. Phenocrysts: beige and green pleocroic zonated clinopyroxene (5%) up to 1.5 mm long, titanite (2%), opaque (1%), nepheline (1%), melilite (1%) and sparse apatite. Presence of sparse zeolite and calcite.
ES-34	Porphyritic texture. Matrix (96%) glassy with opaque, pyroxene and nepheline microlites. Phenocrysts: clinopyroxene (4%) up to 2.5 mm long and opaque (1%).
ES10-2008	Porphyritic texture. Matrix (94%) glassy with opaque and pyroxene microlites. Phenocrysts: beige clinopyroxene (3%) up to 2.5 mm long, opaque (2%), titanite (<1%), nepheline (<1%) and sparse perovskite and apatite.

(continued on next page)

Appendix A (*continued*)

Sample code	Microscopic description
ES14-2008	Porphyritic texture. Matrix (45%) glassy with pyroxene, nepheline and opaque microlites. Phenocrysts: nepheline (30%) up to 2.5×2 mm, clinopyroxene (19%) up to 1.5 mm long, opaque (5%) and sphene (1%). Presence of sparse calcite xenocrysts with leucite inclusion.
ES17-2008	Fluidal glomeroporphyritic texture. Matrix (65%) glassy with nepheline and pyroxene microlites. Phenocrysts: green and beige clinopyroxene (23%) up to 3×1 mm, opaque (6%), nepheline (5%) and perovskite (1%). Presence of autholiths (neph + CPX + opaque).
ESMT-2	Seriated porphyritic texture. Matrix (30%) glassy with nepheline, pyroxene and opaque microlites. Phenocrysts: nepheline (50%) up to 4×3.5 mm, clinopyroxene (15%) up to 4×1 mm, opaque (5%), perovskite (2%) and minor apatite. Presence of two autholiths (neph + CPX + opaque + perovskite) one aphanitic and one phaneritic.
ESMT-4	Fluidal porphyritic texture. Microcrystalline matrix (30%) with nepheline, pyroxene and melilite into sparse glass. Phenocrysts: nepheline (46%) up to 4×2 mm, clinopyroxene (18%) up to 3.5 mm long, titanite (3%), opaque (2%) and apatite (1%). Presence of minor calcite and zenolite plugs.
ESMT-5	Porphyritic texture. Matrix (60%) glassy with few nepheline, pyroxene and opaque microlites. Phenocrysts: clinopyroxene (21%) up to 3×2 mm, nepheline (12%), opaque (6%) and apatite (1%). Presence of minor calcite and zenolite plugs.
ESMT-6	Porphyritic texture. Microcrystalline matrix (30%) with pyroxene, opaque and nepheline microlites. Phenocrysts: clinopyroxene (60%) up to 5×2.5 mm, opaque (8%) and iddingsitized olivine (2%). Presence of minor calcite and zenolite plugs.
ESMT-7	Porphyritic texture. Microcrystalline matrix (30%) with nepheline, opaque and pyroxene microlites. Phenocrysts: clinopyroxene (59%) up to 5.5×2 mm, opaque (8%) and iddingsitized olivine (3%).

Appendix B

Pb isotopic ratio measurements by Multiple Collector Inductively Coupled Mass Spectrometry (MC-MS-ICPMS).

An alternative procedure to the TIMS to measure Pb isotopes at Rutgers using a Fisons PLASMA 54 multi-collector magnetic sector double focusing Inductively Coupled Mass Spectrometer (MC-MS-ICPMS) was developed and employed for some of the samples (Table 3). A detailed description of the instrument design can be found elsewhere (Halliday et al., 1995, 1998; Walder and Freedman, 1992). In general, the instrument combines a double focusing magnetic sector mass spectrometer with an ICP source. The instrument is equipped with a nine-collector Faraday array and is configured with an additional 30-cm radius Electro Static Analyzer (ESA) filter and a Daly detector with ion-counting capability. The abundance sensitivity achieved with the additional ESA energy filter is less than 0.3 ppm (measured as the contribution of mass 238 to mass 237 signals).

In this procedure we measured Pb (204, 206, 207, and 208) and Tl (203 and 205) isotopes. The samples were collected after an ion-exchange chromatography and were dried down and redissolved with 1 ml of 0.5 N HNO_3. An aliquot of processed sample (containing about 1 μg total Pb) was diluted to 2–3 ml with 2% ultrapure (Fisher Optima Grade) Nitric acid and spiked with about 30 μl of Tl standard (~50 ppm).

For sample introduction we used the ARIDUS II (PFA) fitted with a 100 μl/min PFA micro nebulizer (CETAC Inc.) Typical total signal sensitivity is about 2 e^{-11} A for a 200 ppb Pb solution. Typical analysis time was about 20 min (100 ratio measurements). Faraday collectors were dedicated to masses 202, 203, 204 (axial), 205, 206, 207, and 208. In the presence of Hg, measurement of ^{202}Hg is used to correct for the contribution of ^{204}Hg to the total 204 beam intensity. Mass fractionation was determined by comparison of the 205/203 measured ratio with the theoretical value of 2.3871. Measurement precision (2 sigma) of the 208/204 207/204, and 206/204 ratios is about 200 ppm and about 100 ppm for the 208/206 and 207/206 ratios based on repeated measurements of standard NIST 981. An aliquot of NIST 981 was processed though the ion-exchange chromatography in order to confirm the absence of contamination and/or artifacts from sample dissolution and separation. The 981 measurements were consistent with the values reported by Platzner et al. (2001) confirming the absence of cross contamination and they have been included in the average of NIST 981 presented in Table 3.

References

Adam, J., Green, T.H., Sie, S.H., 1993. Proton microprobe determined partitioning pf Rb, Sr, Ba, Y, Zr, Nb and Ta between experimentally produced amphiboles and silicate melts with variable F content. Chemical Geology 109, 29–49.

Albarède, F., Luais, B., Fitton, G., Semet, M., Kaminski, E., Upton, B.G.J., Bachèlery, P., Cheminée, J.L., 1997. The geochemical regimes of Piton de la Fournaise volcano (Réunion) during the last 530,000 years. Journal of Petrology 38, 171–201.

Aulbach, S., Rudnick, R.L., McDonough, W.F., 2008. Li–Sr–Nd isotope signatures of the plume and cratonic lithospheric mantle beneath the margin of the rifted Tanzanian craton (Labait). Contributions to Mineralogy and Petrology 155, 79–92.

Aulbach, S., Rudnick, R.L., McDonough, W.F., 2011. Evolution of the lithospheric mantle beneath the East African Rift in Tanzania and its potential signatures in rift magmas. In: Beccaluva, L., Bianchini, G., Wilson, M. (Eds.), Volcanism and Evolution of the African Lithosphere: Geological Society of America Special Paper, 478, pp. 105–125.

Bagdasaryan, G.P., Gerasimovskiy, V.I., Polyakov, A.I., Gukasyan, R.K., 1973. Age of volcanic rocks in the rift zones of East Africa. Geochemistry International 10, 66–71.

Baker, B.H., Mohr, P.A., Williams, L.A., 1972. Geology of the Eastern Rift System of Africa. Geological Society of America, Special Publications, 36.

Baker, J., Snee, L., Menzies, M., 1996. A brief Oligocene period of flood volcanism in Yemen: implications for the duration and rate of continental flood volcanism at the Afro-Arabian triple junction. Earth and Planetary Science Letters 138, 39–55.

Bell, K., Simonetti, A., 1996. Carbonatite magmatism and plume activity: implications from the Nd, Pb and Sr isotope systematics of Oldoinyo Lengai. Journal of Petrology 37, 1321–1339.

Bell, K., Simonetti, A., 2010. Source of parental melts to carbonatites — critical isotopic constraints. Mineral Petrology 98, 77–89.

Bell, K., Tilton, G., 2001. Nd, Pb and Sr isotopic compositions of East African carbonatites: evidence for mantle mixing and plume inhomogeneity. Journal of Petrology 42, 1927–1945.

Berlund, M., Wieser, M.E., 2011. Isotopic compositions of the elements 2009 (IUPAC Technical Report). Pure and Applied Chemistry 83, 397–410.

Carr, M.J., Saginor, I., Alvarado, G.E., Bolge, L.L., Linsday, F.N., Milidakis, K., Turrin, B.D., Feigenson, M.D., Swisher III, C.C., 2007. Element fluxes from the volcanic front of Nicaragua and Costa Rica. Geochemistry, Geophysics, Geosystems 8, 1–22.

Chesley, J.T., Rudnick, R.L., Lee, C.T., 1999. Re–Os systematics of mantle xenoliths from the East African Rift: age, structure, and history of the Tanzanian craton. Geochimica et Cosmochimica Acta 63, 1203–1217.

Chrorowicz, J., 2005. The East African rift system. Journal of African Earth Sciences 43, 379–410.

Cloutier, J., Stevenson, R.K., Bardoux, M., 2005. Nd isotopic, petrologic and geochemical investigation of the Tulawaka East gold deposit, Tanzanian Craton. Precambrian Research 139, 147–163.

Cohen, R.S., O'Nions, R.K., Dawson, J.B., 1984. Isotope geochemistry of xenoliths from East Africa implications for development of mantle reservoirs and their interaction. Earth and Planetary Science Letters 68, 209–220.

Dalrymple, G.B., Alexander Jr., E.C., Lannphere, M.A., Kraker, G.P., 1981. Irradiation of samples for $^{40}Ar/^{39}Ar$ dating using the Geological Survey TRIGA reactor. U.S. Geological Survey, Professional Paper, 1176.

Dalrymple, G.B., Izett, G.A., Snee, L.W., Obradovich, J.D., 1993. $^{40}Ar/^{39}Ar$ age spectra and total-fusion ages of tektites from Cretaceous–Tertiary boundary sedimentary rocks in the Beloc Formation, Haiti. U.S. Geological Survey Bulletin, 2065.

Davies, G.R., Lloyd, F.E., 1989. Pb–Sr–Nd isotope and trace element data bearing on the origin of the potassic subcontinental lithosphere beneath south-west Uganda. In: Saunders, A.D., Norry, M.J. (Eds.), Kimberlites and Related Rocks, Volume 2: Geological Society of Australia Special Publication, 14, pp. 784–794.

Dawson, J.B., 1992. Neogene tectonics and volcanicity in the North Tanzania sector of the Gregory Rift Valley: contrasts with the Kenya sector. Tectonophysics 204, 81–92.

Dawson, J.B., 2008. The Gregory Rift Valley and Neogene–Recent volcanoes of northern Tanzania. Geological Society, London, Memoirs 33, 1–112.

Dawson, J.B., Smith, J.V., 1988. Metasomatised and veined upper-mantle xenoliths from Pello Hill, Tanzania: evidence for anomalously-light mantle beneath the Tanzanian sector of the East African Rift Valley. Contributions to Mineralogy and Petrology 100, 510–527.

Dawson, J.B., Smith, J.V., 1992. Olivine-mica pyroxenite xenoliths from northern Tanzania: metasomatic products of upper-mantle peridotite. Journal of Volcanology and Geothermal Research 50, 131–142.

Please cite this article as: Mana, S., et al., Geochronology and geochemistry of the Essimingor volcano: Melting of metasomatized lithospheric mantle beneath the North Tanzanian Divergence zone (East African Rift), Lithos (2012), http://dx.doi.org/10.1016/j.lithos.2012.09.009

De Mulder, M., 1985. The Karisimbi Volcano, (Virunga). Musée Royale de l'Afrique Centrale, Tervuren, Belgique Annales. Serie in Octavo Sciences Géologique, 90.
DePaolo, D.J., 1981. Trace element and isotopic effects of combined wallrock assimilation and fractional crystallization. Earth and Planetary Science Letters 53, 189–202.
Downie, C., Wilkinson, P., 1972. The Geology of Kilimanjaro. University of Sheffield, Sheffield.
Dupuy, C., Liotard, J.M., Dostal, J., 1992. Zr/Hf fractionation in the intraplate basaltic rocks: carbonate metasomatism in the mantle source. Geochimica et Cosmochimica Acta 56, 2417–2424.
Ebinger, C.J., Sleep, N.H., 1998. Cenozoic magmatism throughout east Africa resulting from impact of a single plume. Nature 395, 788–791.
Evans, A.L., Fairhead, J.D., Mitchell, J.G., 1971. Potassium–argon ages from the volcanic province of northern Tanzania. Nature 229, 19–20.
Fairhead, J.D., Mitchell, J.G., Williams, L.A., 1972. New K/Ar determinations on rift volcanics of S Kenya and their bearing on age of rift faulting. Nature 238, 66–69.
Foley, S.F., 1993. An experimental study of olivine lamproite: first results from the diamond stability field. Geochimica et Cosmochimica Acta 57, 483–489.
Foley, S.F., Jenner, G.A., 2004. Trace element partitioning in lamproitic magmas — the Gaussberg olivine leucitite. Lithos 75, 19–38.
Fritz, H., Tenczer, V., Hauzenberger, C., Wallbrecher, E., Muhongo, S., 2009. Hot granulite nappes — tectonic styles and thermal evolution of the Proterozoic granulite belts in East Africa. Tectonophysics 477, 160–173.
Furman, T., 1995. Melting of metasomatized subcontinental lithosphere: undersaturated mafic lavas from Rungwe, Tanzania. Contributions to Mineralogy and Petrology 122, 97–115.
Furman, T., Graham, D., 1999. Erosion of lithospheric mantle beneath the East African Rift system: geochemical evidence from the Kivu volcanic province. Lithos 48, 237–262.
Furman, T., Bryce, T., Rooney, T., Hanan, B., Yirgu, G., Ayalew, D., 2006a. (a). Heads and tails: 30 million years of the Afar plume. In: Yirgu, G., Ebinger, C.J., Maguire, P.K.H. (Eds.), The Afar volcanic province in the East African Rift System: Geological Society, Special Publication, London, vol. 256, pp. 95–119.
Furman, T., Kaleta, K.M., Bryce, J.G., Hanan, B.B., 2006b. (b). Tertiary mafic lavas of Turkana, Kenya: constraints on East African plume structure and the occurrence of High-μ volcanism in Africa. Journal of Petrology 47, 1221–1244.
Galer, S.J.G., Abouchami, W., 1998. Practical application of lead triple spiking for correction of instrumental mass discrimination. Mineralogical Magazine 62A, 491–492.
Gazel, E., Carr, M.J., Hoemle, K., Feigenson, M.D., Szymanski, D., Hauff, H., van den Bogaard, P., 2009. Galapagos–OIB signature in southern Central America: mantle refertilization by arc–hot spot interaction. Geochemistry, Geophysics, Geosystems 10, 1–32.
George, R., Rogers, N., Kelley, S., 1998. Earliest magmatism in Ethiopia: evidence for two mantle plumes in one flood basalt province. Geology 26, 923–926.
Halliday, A.N., Lee, D., Christensen, J.N., Walder, A.J., Freedman, P.A., Jones, C.E., Hall, C.M., Yi, W., Teagle, D., 1995. Recent developments in inductively coupled plasma magnetic sector multiple collector mass spectrometry. International Journal of Mass Spectrometry and Ion Processes (Nier Vol) 146 (147), 21–33.
Halliday, A.N., Lee, D., Christensen, J.N., Rehkämper, M., Yi, W., Luo, X., Hall, C.M., BAllentine, C.J., Stirling, C., 1998. Applications of multiple collector-ICPMS to cosmochemistry, geochemistry, and paleoceanography. Geochimica et Cosmochimica Acta 62, 919–940.
Hannan, R.S., Vogel, T.A., Patino, L.C., Alvarado, G.E., Pérez, W., Smith, D.R., 2002. Origin of silicic volcanic rocks in Central Costa Rica: a study of a chemically variable ash-flow sheet in the Tiribí Tuff. Bulletin of Volcanology 64, 117–133.
Hart, S.R., 1984. A large-scale isotope anomaly in the Southern Hemisphere mantle. Nature 309, 753–757.
Hart, S.R., Hauri, E.H., Oschmann, L.A., Whitehead, J.A., 1992. Mantle plumes and entrainment: isotopic evidence. Science 256, 517–520.
Hay, R.L., 1976. Geology of the Olduvai Gorge. Univ. of California Press, Berkeley.
Hayes, S.J., 2004. Magmatic evolution of the Shira volcanics, Mt Kilimanjaro, Tanzania. Ph.D. thesis, Queensland University of Technology.
Hofmann, A.W., Jochum, K.P., Seufert, M., White, W.M., 1986. Nb and Pb in oceanic basalts: new constraints on mantle evolution. Earth and Planetary Science Letters 79, 33–45.
Hofmann, C., Courtilloy, V., Féraud, G., Rochette, P., Yirgu, G., Ketefo, E., Pik, R., 1997. Timing of the Ethiopian flood basalt event and implications for plume birth and global change. Nature 389, 838–841.
Isaacs, G.L., Curtis, G.H., 1974. Age of Early Acheulian industries from the Peninj Group, Tanzania. Nature 249, 624–626.
Jackson, M.G., Dasgupta, R., 2008. Compositions of HIMU, EM1, and EM2 from global trends between radiogenic isotopes and major elements in ocean island basalts. Earth and Planetary Science Letters 276, 175–186.
Kalt, A., Hegner, E., Satir, M., 1997. Nd, Sr, and Pb isotope evidence for diverse lithospheric mantle sources of East African Rift carbonatites. Tectonophysics 278, 31–45.
LaTourette, T., Hervig, R.L., Holloway, J.R., 1995. Trace element partitioning between amphibole, phlogopite, and basanite melt. Earth and Planetary Science Letters 135, 13–30.
Le Gall, B., Nonnotte, P., Rolet, J., Beniot, M., Guillou, H., Mousseau-Nonnotte, M., Albaric, J., Deverchere, J., 2008. Rift propagation at craton margin. Distribution of faulting and volcanism in the North Tanzanian Divergence (East Africa) during Neogene times. Tectonophysics 448, 1–19.
Le Maitre, R.W., Bateman, P., Dudek, A., Keller, J., Lameyre, J., Le Bas, M.J., Sabine, P.A., Schmit, R., Sorensen, H., Streckeisen, A., Woolley, A.R., Zanettin, B., 1989. A Classification of Igneous rocks and Glossary of Terms: Recommendations of the International Union of Geological Sciences Subcommission on the Systematics of Igneous Rocks. Blackwell Scientific, Oxford.
Lee, C.T., Rudnick, R.L., 1999. Compositionally stratified cratonic lithosphere: petrology and geochemistry of peridotite xenoliths from the Labait tuff cone, Tanzania. In: Gurney, J.J., Richardson, S.R. (Eds.), Proceedings of the 7th International Kimberlite Conference, pp. 503–521.
Lin, S., Kuo, B., Chiao, L., van Keken, P.E., 2005. Thermal plume models and melt generation in East Africa: a dynamic modeling approach. Earth and Planetary Science Letters 237, 175–192.
Lloyd, F.E., Arima, M., Edgar, A.D., 1985. Partial melting of a phlogopite–clinopyroxenite nodule from south-west Uganda: an experimental study bearing on the origin of highly potassic continental rift volcanics. Contributions to Mineralogy and Petrology 91, 321–329.
Macdonald, R., Davies, G.R., Upton, B.G.J., Dunkley, P.N., Smith, M., Leat, P.T., 1995. Petrogenesis of Silai volcano, Gregory Rift, Kenya. Journal of the Geological Society of London 152, 703–720.
Macdonald, R., Rogers, N.W., Fitton, J.G., Black, S., Smith, M., 2001. Plume–Lithosphere interactions in the generation of the basalts of the Kenya Rift, East Africa. Journal of Petrology 42, 877–900.
MacIntyre, R.M., Mitchell, J.G., Dawson, J.B., 1974. Age of fault movements in Tanzanian sector of East African Rift System. Nature 247, 354–356.
Mansur, A.T., 2008. Age, composition, and origin of the lower continental crust, northern Tanzania. MS thesis, University of Maryland.
Manya, S., Maboko, M.A.H., Nakamura, E., 2007. The geochemistry of high-Mg andesite and associated adakitic rocks in the Musoma–Mara Greenstone Belt, northern Tanzania: possible evidence for Neoarchean ridge subduction? Precambrian Research 159, 241–259.
McDougall, I., Harrison, T.M., 1999. Geochronology and Thermochronology by the $^{40}Ar/^{39}Ar$ Method. Oxford University Press, New York.
Mollel, G.F., Swisher III, C.C., Feigenson, M.D., Carr, M.J., 2008. Geochemical evolution of Ngorongoro Caldera, northern Tanzania: implications for crust–magma interaction. Earth and Planetary Science Letters 271, 337–347.
Mollel, G.F., Swisher III, C.C., McHenry, L.J., Feigenson, M.D., Carr, M.J., 2009. Petrogenesis of basalt–trachyte lavas from Olmoti Crater, Tanzania. Journal of African Earth Sciences 54, 127–143.
Mollel, G.F., Swisher III, C.C., Feigenson, M.D., Carr, M.J., 2011. Petrology, geochemistry, and age of Satiman, Lemagurut and Oldeani: sources of the volcanic deposits of the Laetoli area. In: Harrison, T. (Ed.), Paleontology and Geology of Laetoli: Human Evolution in Context 1. Springer, Dordrecht.
Möller, A., Mezger, K., Schenk, V., 1998. Crustal age domains and the evolution of the continental crust in the Mozambique Belt of Tanzania: combined Sm–Nd, Rb–Sr, and Pb–Pb isotopic evidence. Journal of Petrology 39, 749–793.
Nonnotte, P., Guillou, H., Le Gall, B., Benoit, M., Cotton, J., Scaillet, S., 2008. New K–Ar age determinations of Kilimanjaro volcano in the North Tanzanian diverging rift, East Africa. Journal of Volcanology and Geothermal Research 173, 99–112.
Nonnotte, P., Benoit, M., Le Gall, B., Hémond, C., Rolet, J., Cotton, J., Brunet, P., Makoba, E., 2011. Petrology and geochemistry of alkaline lava series, Kilimanjaro, Tanzania: new constraints on petrogenetic processes. In: Beccaluva, L.G., Wilson, M. (Eds.), Volcanism and Evolution of the African Lithosphere: Geological Society of America Special Paper, 478, pp. 127–158.
Nyblade, A.A., Owens, T.J., Gurrola, H., Ritsema, J., Langston, C.A., 2000. Seismic evidence for a deep upper mantle thermal anomaly beneath east Africa. Geology 28, 599–602.
O'Hara, M.J., 1968. The Bearing of Phase Equilibria Studies in Synthetic and Natural Systems on the Origin and Evolution of Basic and Ultrabasic Rocks. Earth-Sciences Reviews, Elsevier Publishing Company, Amsterdam . (printed in The Netherlands).
Olafsson, M., Eggler, D.H., 1983. Phase relations of amphibole, amphibole–carbonate, and phlogopite–carbonate peridotite: petrologic constraints on the asthenosphere. Earth and Planetary Science Letters 64, 305–315.
Owens, T.J., Nyblade, A.A., Gurrola, H., Langston, C.A., 2000. Mantle transition zone structure beneath Tanzania, East Africa. Geophysical Research Letters 27, 827–830.
Paslick, C.R., Halliday, A.N., James, D., Dawson, J.B., 1995. Enrichment of the continental lithosphere by OIB melts: isotopic evidence from the volcanic province of northern Tanzania. Earth and Planetary Science Letters 130, 109–126.
Pike, J.E.N., Meyer, C.E., Wilshire, H.G., 1980. Petrography and chemical composition of a suite of ultramafic xenoliths from Lashaine, Tanzania. Journal of Geology 88, 343–352.
Platz, T., Foley, S.F., André, L., 2004. Low-pressure fractionation of the Nyiragongo volcanic rocks, Virunga Province, D.R. Congo. Journal of Volcanology and Geothermal Research 136, 269–295.
Platzner, I., Ehrlich, S., Halicz, L., 2001. Isotope-ratio measurements of lead in NIST standard reference materials by multiple-collector inductively coupled plasma mass spectrometry. Fresenius' Journal of Analytical Chemistry 370, 624–628.
Renne, R., Swisher III, C.C., Deino, A., Kamer, D., Owens, T., DePaolo, D., 1998. Intercalibration of standards, absolute ages, and uncertainties in $^{40}Ar/^{39}Ar$ dating. Chemical Geology 145, 117–153.
Rogers, N.W., De Mulder, M., Hawkesworth, C.J., 1992. An enriched mantle source for potassic basanites: evidence from Karisimbi volcano, Virunga volcanic province, Rwanda. Contributions to Mineralogy and Petrology 111, 543–556.
Rogers, N.W., James, D., Kellet, S.P., De Mulder, M., 1998. The generation of potassic lavas from the Eastern Virunga province, Rwanda. Journal of Petrology 39, 1223–1247.
Rogers, N., Macdonald, R., Fitton, J.G., George, R., Smith, M., Barreiro, B., 2000. Two mantle plumes beneath the East African rift system: Sr, Nd and Pb isotope evidence from Kenya Rift basalts. Earth and Planetary Science Letters 176, 387–400.
Rollinson, H.R., 1993. Using Geochemical Data: Evaluation, Presentation, Interpretation. Pearson Education, Essex, UK, p. 352.
Rosenthal, A., Foley, S.F., Pearson, D.G., Nowell, G.M., Tappe, S., 2009. Petrogenesis of strongly alkaline primitive volcanic rocks at the propagating tip of the western branch of the East African Rift. Earth and Planetary Science Letters 284, 236–248.

Please cite this article as: Mana, S., et al., Geochronology and geochemistry of the Essimingor volcano: Melting of metasomatized lithospheric mantle beneath the North Tanzanian Divergence zone (East African Rift), Lithos (2012), http://dx.doi.org/10.1016/j.lithos.2012.09.009

Rudnick, R.L., Fountain, D.M., 1995. Nature and composition of the continental crust: a lower crustal perspective. Reviews of Geophysics 33, 267–309.
Rudnick, R.L., Gao, S., 2003. Composition of the continental crust. In: Rudnick, R.L. (Ed.), The Crust. In: Holland, H.D., Turekian, K.K. (Eds.), Treatise on Geochemistry, 3. Elsevier, Oxford, pp. 1–64.
Rudnick, R.L., McDonough, W.F., Chappell, B.W., 1993. Carbonatite metasomatism in the northern Tanzanian mantle: petrographic and geochemical characteristics. Earth and Planetary Science Letters 114, 463–475.
Sack, R.O., Walker, D., Carmichael, I.E.S., 1987. Experimental petrology of alkali lavas: constraints on cotectics of multiple saturation in natural basic liquids. Contributions to Mineralogy and Petrology 96, 1–23.
Sato, K., Katsura, T., Ito, E., 1997. Phase relations of natural phlogopite with and without enstatite up to 8 GPa: implication for mantle metasomatism. Earth and Planetary Science Letters 146, 511–526.
Shaw, D.M., Cramer, J.J., Higgins, M.D., Truscott, M.G., 1986. Composition of the Canadian Precambrian shield and the continental crust of the Earth. In: Dawson, J.B., Carswell, D.A., Hall, J., Wedepohl, K.H. (Eds.), The Nature of the Lower Continental Crust: Geological Society of London, London, 24, pp. 257–282.
Smith, M., 1994. Stratigraphic and structural constraints on mechanisms of active rifting in the Gregory Rift, Kenya. Tectonophysics 236, 3–22.
Sun, S.S., McDonough, W.F., 1989. Chemical and isotopic systematic of oceanic basalts: implications for mantle composition and processes. In: Saunders, A.D., Norry, M.J. (Eds.), Magmatism in the Oceanic Basins: Geological Society Special Publication, 42, pp. 313–345.
Taylor, S.R., McLennan, S.M., 1985. The Continental Crust: Its Composition and Evolution. Blackwell, Oxford.
Taylor, S.R., McLennan, S.M., 1995. The geochemical evolution of the continental crust. Reviews of Geophysics 33, 241–265.
Walder, A.J., Freedman, P.A., 1992. Isotopic ratio measurement using a double focusing magnetic sector mass analyzer with an inductively coupled plasma as an ion source. Journal of Analytical Atomic Spectrometry 7, 571–575.
Weeraratne, D.S., Forsyth, D.W., Fisher, K.M., 2003. Evidence for an upper mantle plume beneath the Tanzania craton from Rayleigh wave tomography. Journal of Geophysical Research 108, 1–17.
Wilkinson, P., Mitchel, J.G., Cattermole, P.J., Downie, C., 1986. Volcanic chronology of the Meru–Kilimanjaro region, northern Tanzania. Journal of the Geological Society of London 143, 601–605.
Wood, C.P., 1968. A geochemical study of East African alkaline lavas and its relevance to the petrogenesis of nephelinites. Ph.D thesis, University of Leeds.
Workman, R.K., Hart, S.R., Jackson, M., Regelous, M., Farley, K.A., Blusztajn, J., Kurz, M., Staudigel, H., 2004. Recycled metasomatized lithosphere as the origin of the enriched mantle II (EM2) end-member: evidence from the Samoan volcanic chain. Geochemistry, Geophysics, Geosystems 5, 1–44.
Zindler, A., Hart, S., 1986. Chemical geodynamics. Annual Review Earth and Planetary Science 14, 493–571.

Please cite this article as: Mana, S., et al., Geochronology and geochemistry of the Essimingor volcano: Melting of metasomatized lithospheric mantle beneath the North Tanzanian Divergence zone (East African Rift), Lithos (2012), http://dx.doi.org/10.1016/j.lithos.2012.09.009